Project-thesis

Influence of oxygen stoichiometry onto physical properties of $La_{0.7}Sr_{0.3}MnO_{3-\delta}$ thin films and $La_{0.7}Sr_{0.3}MnO_{3-\delta}$ Powder

August 2021

In JCNS-2, Forschungszentrum Jülich

By Chenyang Yin from RWTH Aachen

Supervised by

Prof. Dr. Thomas Brückel

PD Dr. Oleg Petracic

Zusammenfassung

Die Sauerstoffstöchiometrie kann einen großen Einfluss auf die physikalischen Eigenschaften komplexer Oxide haben. In einer früheren Untersuchung wurde die durch Sauerstofffehlstellen induzierte topotaktische Phasenumwandlung in dünnen Schichten von $La_{0.7}Sr_{0.3}MnO_{3-\delta}$ (LSMO) erfolgreich mittels Vakuum-Postannealing durchgeführt. In dieser Arbeit werden LSMO-Dünnschichten mittels Hochdruck-Sauerstoff-Sputtern bei den zuvor bestimmten optimalen Wachstumsparametern aufgewachsen. Um ein besseres Verständnis der abweichenden Sauerstoff-Stöchiometrie in LSMO-Dünnschichtsystemen zu erhalten und die topotaktische Phasenumwandlung zu realisieren, wird der Einfluss eines angelegten elektrischen Feldes mittels einer ionischen Flüssigkeit ('ionic liquid gating') eingesetzt. Andere Studien an der verwandten Verbindung $LaSrCoO_3$ weisen eine außerordentlich hohe Effizienz bei der Auslösung der Phasenumwandlung hin. Bei ausreichend großen Gating-Spannungen wird mittels Röntgendiffraktometrie eine signifikante Gitteraufweitung gefunden, die durch Wasserstoffeinlagerung oder Sauerstofffehlstellenbildung verursacht wird. Darüber hinaus wird auch eine durch 'Ionic Liquid Gating' induzierte Filmzersetzung mittels Rasterkraftmikroskopie beobachtet. Die magnetischen Eigenschaften wurden ebenfalls nach der Behandlung ermittelt. Eine starke Verringerung der Magnetisierung sowie eine niedrigere Curie-Temperatur weisen auf eine unterdrückte Doppelaustausch-Wechselwirkung hin. Zusätzlich wird der tiefenaufgelöste Wasserstoffgehalt in den Filmen mittels Kernreaktionsanalyse quantifiziert.

Verglichen mit dem verspannten System (d.h. Dünnschichten) hat die systematische Untersuchung des topotaktischen Phasenumwandlungs in einem unverspannten System (d.h. Bulk-Pulver) weniger Aufmerksamkeit erhalten. Daher wird im zweiten Teil dieser Arbeit LSMO-Pulver untersucht. Die Pulverproben wurden durch mechanisches Mahlen eines alten Sputtern-Targets präpariert und anschließend unter verschiedenen Vakuum-Bedingungen Aluminium-unterstützt ausgeheizt. Die Ergebnisse zeigen einen Weg auf, um die topotaktische Phasenumwandlung von Perowskit zu Brownmillerit über einen Zwischenzustand mit antiferromagnetischem Verhalten herbeizuführen.

Abstract

Oxygen stoichiometry can exhibit a large influence onto the physical properties of complex oxides. In a previous study, the oxygen vacancy induced topotactic phase transition in $La_{0.7}Sr_{0.3}MnO_{3-\delta}$ (LSMO) thin films was successfully triggered by vacuum annealing. In this thesis, LSMO thin films are prepared by High Oxygen Pressure Sputter Deposition (HOSPD) with the optimal growth parameters as determined before. To obtain a deeper understanding of oxygen off- stoichiometry in LSMO thin film systems as well as to trigger the topotactic phase transition, ionic liquid gating (ILG) is employed. Other studies on the related compound $LaSrCoO_3$ indicate an extraordinarily high efficiency for triggering the phase transition. Under sufficiently large gating voltages, a significant lattice expansion triggered by hydrogen insertion or oxygen vacancy formation is found from X-ray diffractometry. Moreover, a film decomposition induced by ILG is also observed using atomic force microscopy (AFM). The magnetic properties are also determined after ILG. A large reduction of the magnetization as well as a lower Curie temperature indicate suppressed double exchange interactions. In addition, the depth resolved hydrogen content in the films is quantified using nuclear reaction analysis (NRA).

Compared with the strained system (i.e. thin film), the systematic study of the topotactic phase transition in an unstrained system (i.e. bulk powder) has received less attention. Therefore, in the second part of this thesis, LSMO bulk powder is studied. The powder samples are prepared by hand milling using an old HOPSD target. Then aluminum-assisted vacuum annealing is performed at various conditions. The results reveal a route for the perovskite-to-brownmillerite topotactic phase transition via an intermediate state showing anti-ferromagnetic behavior.

Contents

1. Introduction

The physical properties of complex oxides can be drastically influenced by its oxygen stoichiometry. By systematically changing the oxygen stoichiometry the intrinsic influence of oxygen vacancies onto the physical properties can be studied. In a multivalent system such as transition metal ions their oxidation number can be tuned, which in turn also governs the physical properties. Consequently, complex oxides offer the tunability of lattice structure, electric transport and magnetic properties and thus enabling potential applications e.g. as solid fuel cells, catalysts, and memristors [1, 2, 3].

In LSMO also altering the La to Sr ratio controls various properties. In this thesis, $La_{0.7}Sr_{0.3}MnO_{3-\delta}$ (δ represents the potential deviation during growth) is chosen due to its room temperature ferromagnetic and metallic behavior and its relatively high Curie temperature. Moreover, LSMO exhibits sponge-like oxygen loading and unloading abilities. Also, the oxygen vacancy induced topotactic phase transition from the initial perovskite phase (PV) to the layered vacancy ordered brownmillerite (BM) phase and vice versa can be easily triggered. This phase transition is accompanied by a transition from ferromagnetic to anti-ferromagnetic as well as from metallic to insulating behavior [4]. In this study, thin film samples are prepared by High Oxygen Pressure Sputter Deposition (HOPSD). Also, an old target with the same stoichiometry is used to prepare bulk powder by hand milling. Moreover, ionic liquid gating is employed to change the physical properties of the thin film samples. The results indicate a lattice expansion under ionic liquid gating as well as the suppression of the double exchange interactions leading to a weakened ferromagnetic behavior. For the powder sample, the PV to BM topotactic phase transition is triggered successfully by aluminum-assisted annealing.

Outline of this thesis

The theoretical background is introduced in **chapter 2**. First, the lattice structure of perovskites as well as transition metal oxides is described. Then, the background of magnetism in transition metal oxides is highlighted. Considering the sample preparation and structural characterization, typical thin film growth methods as well as the scattering theory is shortly mentioned. In **chapter 3** the corresponding experimental methods and instruments are shown. **Chapter 4** focuses on the ionic liquid gating method

on the thin film samples. The topotactic phase transition triggered by aluminum-assisted vacuum annealing based on the powder sample is presented in **chapter 5**.

2. Theoretical Background

In this chapter the theoretical backgrounds involved in this thesis are discussed. First, the perovskite structure and its variant brownmillerite are introduced, followed by a description of the transition metal oxide LSMO. Then the magnetism in transition metal oxides is mentioned e.g. crystal field splitting and exchange interactions. Finally, the corresponding growth methods and the scattering theory are described.

2.1 Perovskite structure and variants

2.1.1 ABO_3 Perovskite

The perovskite is a typical mineral with the formula of $CaTiO_3$, which was found in the 19th century by the Prussian mineralogist Gustav Rose. The name "perovskites" is adopted by the compounds which have the chemical stichometry ABO_3. Typically, $SrTiO_3$ exhibits ideal cubic perovskite structure with space group $Pm\bar{3}m$ as shown in **Figure 2.1**. The eight corners of the unit cell (A-site) are occupied by alkaline earth metal cations or rare earth cations with larger ionic radius. With smaller radius, the transition metal cations are located at the center of the unit cell and surrounded by an oxygen octahedron. Due to the flexible potential substitutions at the A- and B-sites and their rich physical properties, perovskites are intensively studied.

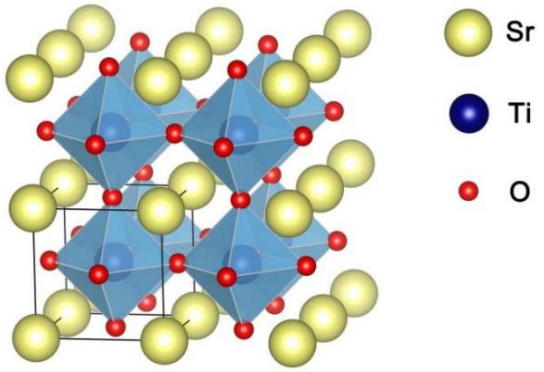

Figure 2.1 Crystal structure of $SrTiO_3$, showing eight unit cells. Figure taken from Ref [4].

2.1.2 Brownmillerite

The mineral brownmillerite with the chemical composition $Ca_2(Al, Fe)_2O_5$ was found in 1932. The brownmillerite structure ($ABO_{2.5}$) can be described as an oxygen deficient perovskite with alternating oxygen tetrahedra and octahedra. By forming of oxygen vacancies in the [110] direction, the original perovskite structure can be transformed to brownmillerite by a topotactic phase transition.

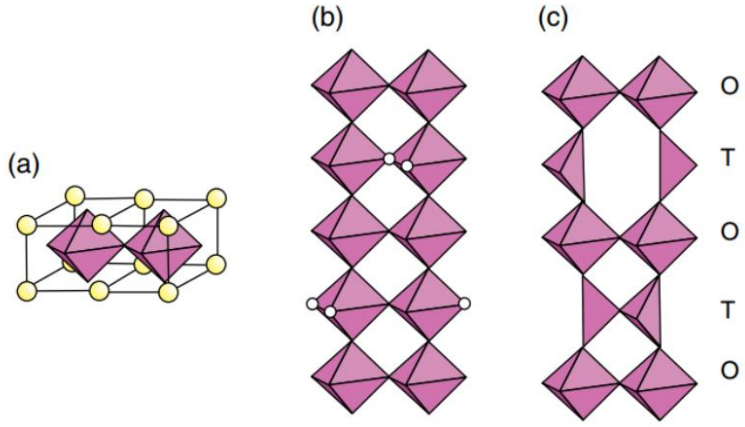

Figure 2.2 Crystal structure of $ABO_{2.5}$ Brownmillerite, figure taken from [5]. Oxygen vacancies are in the [110] direction, thus showing alternating oxygen octahedra and tetrahedra.

2.2 Transition metal oxides

Among complex oxides, transition metal oxides with a magnetic element show unique tunable electric, magnetic, and spintronic properties. This enables various functionalities in many applications [6, 7, 8]. Recently, the multivalent transition metal oxide $La_{1-x}Sr_xMnO_3$ has attracted intense attention due to its tunable physical properties by various Sr doping concentrations. By tuning the Mn oxidation state via Sr doping, LSMO can show different magnetic ordering phenomena, in particular ferromagnetic (FM) and antiferromagnetic (AFM) ordering (**Figure 2.3 (a)**).

In **Figure 2.3 (b)**, the phase diagram is depicted for various Sr doping [9]. When zero doped, i.e. for $LaMnO_3$ one finds A-type AFM spin order at low temperatures companied with an insulating behavior. Here the Mn ion only occurs in the Mn^{3+} oxidation state. Upon increasing the Sr content, the Mn^{3+} is gradually replaced by Mn^{4+}. The La to Sr ratio corresponds to the ratio of Mn^{3+} to Mn^{4+}. In the range of $0.1<x<0.5$, a FM phase emerges. For $x=0.175$, with the vanishing of a Jahn-Teller distortion and appearing of rhombohedral structure, the system is transformed from insulating to metallic behavior

[10]. For 0.5<x<0.6, the system returns to A-type AFM ordering and behaves metallic at lower temperatures and displays FM and metallic behavior at higher temperatures [11]. With larger Sr doping (0.7<x<0.85), C-type AFM ordering and insulating behavior emerges. Besides stoichiometry, strain caused by the substrate in epitaxial thin film system can also introduce large influences onto the physical properties.

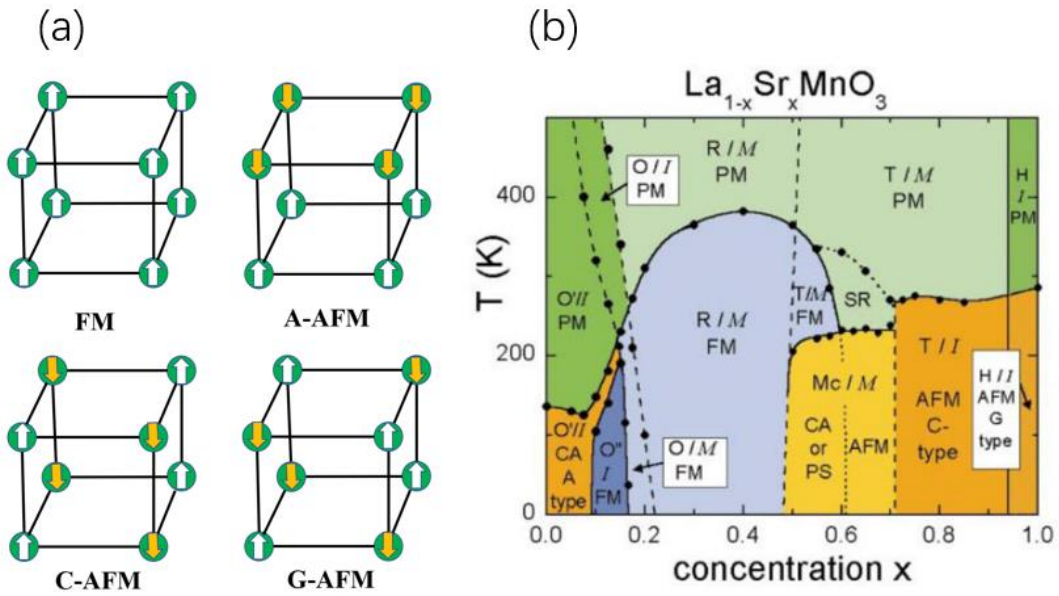

Figure 2.3 (a) Typical schematic AFM and FM spin ordering. (b) Phase diagram of $La_{1-x}Sr_xMnO_3$. Regarding the crystal structure, symbols O, O', O", R, T, H, and M_C are used to represent orthorhombic, Jahn-Teller distorted orthorhombic, orbital-ordered orthorhombic, rhombohedral, tetragonal, hexagonal, and monoclinic, respectively. Regarding the magnetic and electric transport property, the abbreviations mean PA: paramagnetic, FM: ferromagnetic, AFM: antiferromagnetic, M: metallic, and I: insulating. Figure taken from Ref [9].

In this thesis, we choose to study the $La_{0.7}Sr_{0.3}MnO_3$ system. In this stoichiometry, the Mn^{3+} and Mn^{4+} coexist at the ratio of 0.7 : 0.3. This system shows a perovskite type (ABO_3) rhombohedral structure ($R\bar{3}c$). It is ferromagnetic and metallic at room temperature with a bulk Curie temperature of 365 K. The basic crystal structure of $La_{0.7}Sr_{0.3}MnO_3$ is shown in **Figure 2.4**. The Mn^{3+} and Mn^{4+} ions are located at the center of the unit cell and are surrounded by an oxygen octahedron. The eight corners of the unit cell are occupied by La^{3+} and Sr^{2+}.

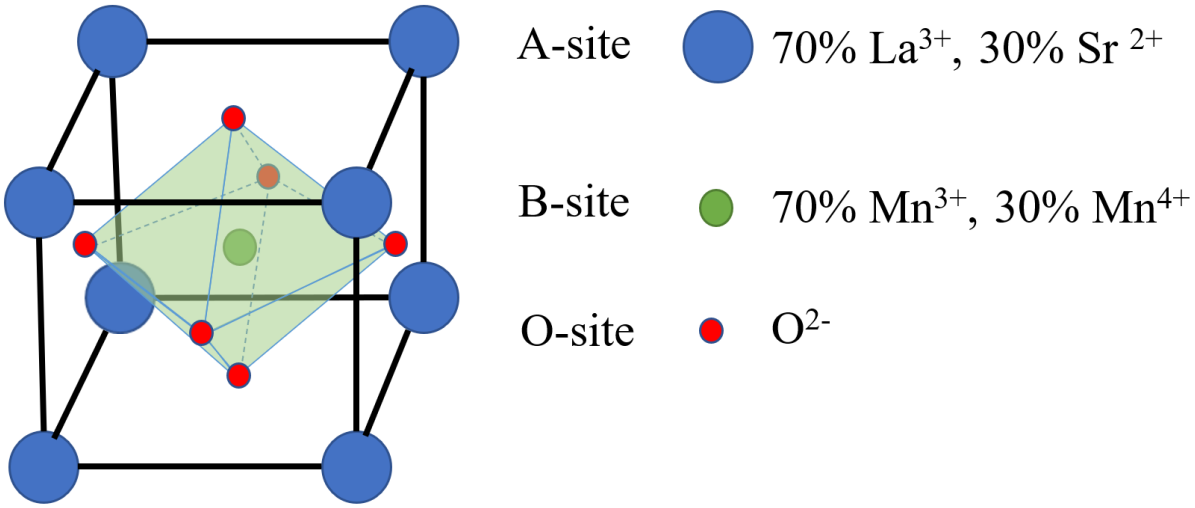

Figure 2.4 Basic structure of $La_{0.7}Sr_{0.3}MnO_3$ in perovskite type pseudocubic structure with space group $R\bar{3}c$. A-sites are occupied by lanthanum and strontium. B, and C sites are occupied by manganese and oxygen, respectively.

2.3 Magnetism in transition metal oxides

For transition metal oxides, the electronic and magnetic properties are mainly influenced by the d-electrons of the transition metal. In this subsection, both crystal field splitting as well as exchange interactions involved in the LSMO system are introduced. In neutral manganese atoms the $[Ar]3d^5 4s^2$ configuration is adopted.

2.3.1 Crystal field splitting

At the center of the unit cell, the 3d-orbitals of manganese ion are split from the original degenerate states (free ion) into e_g $(d_{z^2}, d_{x^2-y^2})$ orbitals and t_{2g} (d_{xy}, d_{xz}, d_{yz}) orbitals due to the electric field applied by the surrounding oxygen ligands, termed crystal field splitting [12]. A crystal field splitting energy Δ (around 2 eV) is introduced which depend on the Mn-O distance [13]. Due to the small value of Δ in our system the 3d-electrons are energetically more favorable to occupy both e_g and t_{2g} orbitals according to Hund's rules and resulting in a high spin state as illustrated in **Figure 2.5**. Moreover, the lattice can be distorted spontaneously in order to achieve a lower total energy by further lifting the degeneracy of the e_g and t_{2g} orbitals, called Jahn- Teller distortion.

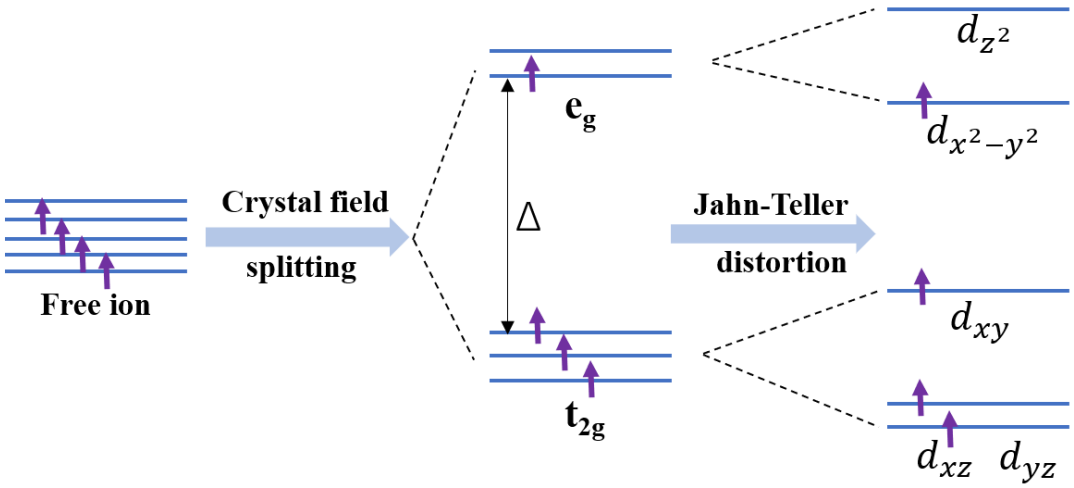

Figure 2.5 3d-orbitals of a Mn^{3+} ion under crystal field splitting and Jahn-Teller distortion.

2.3.2 Super-exchange and double-exchange interactions

For manganites, the exchange interactions between 3d-electrons of the manganese ions occurs via oxygen bridges and dominate the magnetic properties of the compound. As shown in **Figure 2.6 (a)**, the 3d-electrons of the manganese ion at the same oxidation state (Mn^{3+}) can be aligned to an antiferromagnetic spin ordering via the intermediate oxygen anions by super-exchange interactions. Furthermore, when the manganese ions show different valences (e.g. Mn^{3+} and Mn^{4+} in **Figure 2.6 (b)**), the hopping of 3d-electrons through oxygen bridges enables a ferromagnetic spin configuration as well as metallic behavior, called double-exchange interactions.

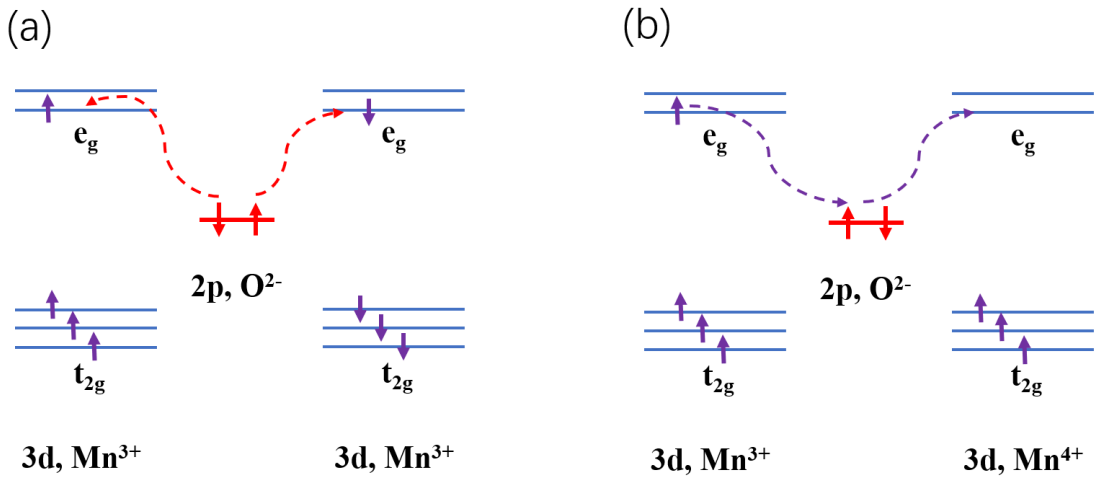

Figure 2.6 (a) Super-exchange interactions between Mn^{3+}. (b) Double-exchange interactions between Mn^{3+} and Mn^{4+}.

2.4 Thin film growth

Nowadays thin film technology enables a large variety of applications in modern society, e.g., LEDs for energy efficient lighting or potentially in future memristors for integrated circuits [14]. The performance of thin films is significantly affected by the growth method. Hence, a comprehensive understanding of typical thin film growth methods as well as of the various growth mechanisms is important.

2.4.1 CVD&PVD methods

The most often employed methods for thin film growth are chemical vapor deposition (CVD) and physical vapor deposition (PVD). In CVD, the thin film is grown by a chemical reaction of vapor precursors at the surface of the substrate. In addition to traditional CVD, metal-organic CVD (MOCVD) as well as atomic layer deposition (ALD) has received widespread attention. For PVD, the atoms or molecules are evaporated from a condensed phase to a vapor phase and then re-condense back on the substrate surface. Here the typical evaporation methods are: i) evaporation by phonon or electron beam heating (e.g. in MBE), ii) sputtering by ion bombardment (e.g. in HOPSD), iii) evaporation by photon bombardment (e.g. in PLD).

2.4.2 Deposition growth modes

The thin film growth process in PVD can be described as following. First, atoms or molecules are ejected by various methods into the vapor phase, then they are bonded by chemisorption (chemical bonding) or physisorption (e.g. Van der Waals bonding) on the substrate followed by surface diffusion to more energetic favorable sites. The nucleation and growth can then lead to epitaxial thin films. Depending on different substrates the growth can be classified into: homoepitaxial growth (the material of the thin film is the same as the material of the substrate) or heteroepitaxial growth (the material of thin film and of the substrate are different).

For homoepitaxial growth the modes are: i) step flow growth, ii) layer-by-layer growth, iii) island growth by second layer nucleation due to a large Ehrlich-Schwoebel barrier. As illustrated in **Figure 2.7**, for heteroepitaxial growth, as also employed in this thesis, three typical growth modes exit, which

can be distinguished from each other by relations between the surface free energy: i) Frank-van-der-Merve mode, ii) Volmer-Weber mode, iii) Stranski-Krastanov mode [15, 16].

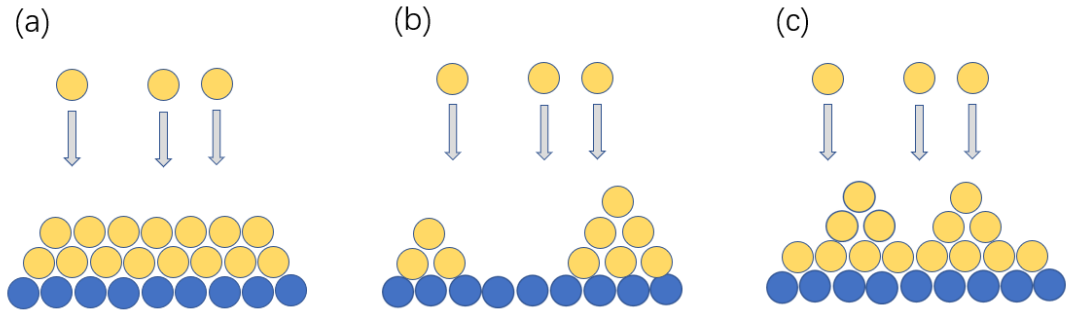

Figure 2.7 Growth modes of heteroepitaxial growth. (a) Frank-van-der-Merve mode, $\gamma_{film} + \gamma_{inter} < \gamma_{sub}$. (b) Volmer-Weber mode, $\gamma_{film} + \gamma_{inter} > \gamma_{sub}$. (c) Stranski-Krastanov mode, $\gamma_{film} + \gamma_{inter} + \gamma_{mis} > \gamma_{sub}$.

When the sum of the thin film surface free energy γ_{film} and the interface free energy γ_{inter} is smaller than the substrate free energy γ_{sub}, it is energetically more favorable for the atoms to bond to the substrate rather than to each other, thus a layer-by-layer growth called Frank-van-der-Merve mode is resulting and hence a smooth film surface. However, when $\gamma_{film} + \gamma_{inter} > \gamma_{sub}$, the Volmer-Weber mode is found and leads to 3D island growth with increased roughness. In between, the influence of the misfit free energy γ_{mis} can exhibit a strong influence, e.g. when reaching a critical thickness. Then the growth mode changes from layer-by-layer growth to island growth in order to relax the accumulated strain due to a lattice misfit. Such a mixed growth mode is called Stranski-Krastanov mode.

2.5 Scattering theory

In this thesis, X-ray diffraction and X-ray reflectivity is used to characterize the lattice structure and film thickness. In this subsection, the basic theory of scattering as well as the fundamental principles of X-ray diffractometry and reflectometry are introduced. Since the sample size is far smaller than the source-sample and sample-detector distance (**Figure 2.8)**, Fraunhofer diffraction (i.e. far-field diffraction with plane waves at the object and the observer) is assumed according to **Equation 2-1**. The R refers to the distance between diffracting object and observation plane, the D and λ refer to the object diameter and the wavelength, respectively. Additionally, elastic scattering is assumed. Thus, the incident and the scattered wave have the same wavelength as described in **Equation 2-2**, the $\vec{k}$ and $\vec{k}'$

represent wave vector before and after scattering, respectively. Moreover, the corresponding relation between the scattering vector $\vec{Q}$ and the wave vector is shown is **Equation 2-3**

$$R \gg D^2 \div \lambda \tag{2-1}$$

$$|\vec{k}| = |\vec{k'}| = \frac{2\pi}{\lambda} \tag{2-2}$$

$$Q = |\vec{Q}| = |\vec{k'} - \vec{k}| = \sqrt{(\vec{k'} - \vec{k})^2} = \frac{4\pi sin\theta}{\lambda} \tag{2-3}$$

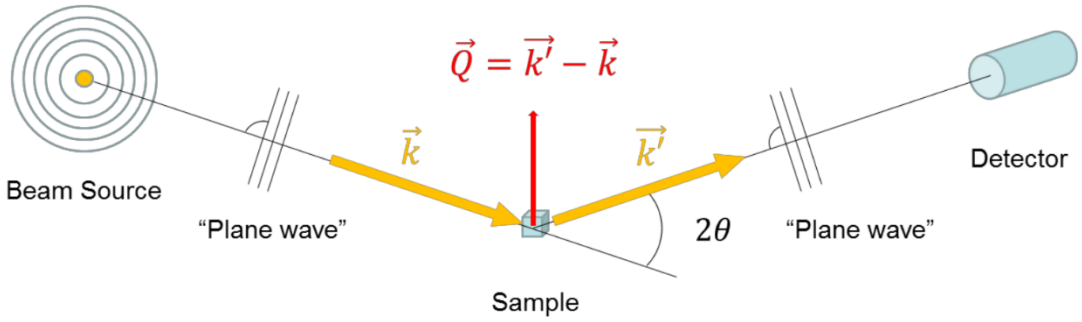

Figure 2.8 Scattering in the Fraunhofer diffraction approximation. Figure taken from Ref [17].

2.5.1 Diffractometry

X-ray diffractometry can be employed to characterized periodic crystal structures due to the similar length scale between the X-ray wavelength and the lattice parameters. The Bragg equation (**Equation 2-4**) describes the condition for constructive interference, which is that the propagation distance difference equals the integer number of the incident wavelength (λ). The lattice spacing is d.

$$2d \times sin\theta = n \times \lambda \tag{2-4}$$

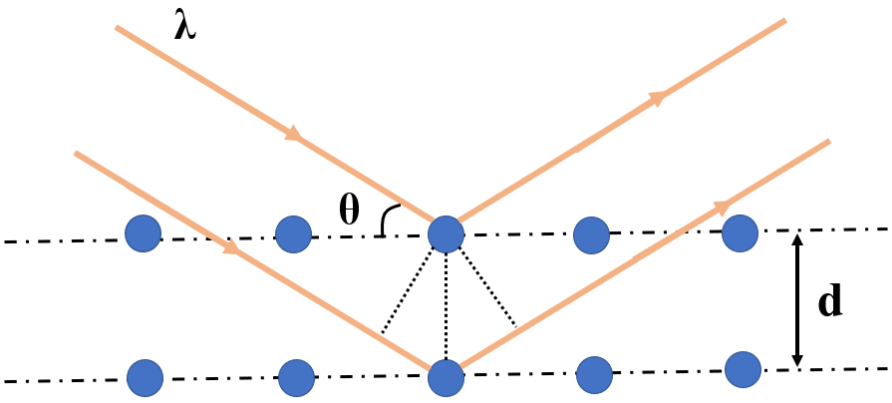

Figure 2.9 Sketch of X-ray scattering in a crystal lattice.

2.5.2 Reflectometry

Reflectometry is widely used for thin film surface and interface characterization. At grazing incidence, and below the critical angle θ_c, the incident X-ray beam undergoes total reflection on the material surface with refraction index $n < 1$. The critical angle can be calculated using **Equation 2-5**, the ρ refers to the electron density of the material [18].

$$\theta_c = arcsin(1/n) \cong \lambda\sqrt{\frac{\rho}{\pi}} \tag{2-5}$$

When the incident angle is above θ_c, the incident beam can be partially transmitted toward the film. Assuming an ideally flat film surface, the reflected intensity is reduced by a factor of Q^{-4}. Moreover, interference can occur for the reflected beam by the film surface and the film-substrate interface as shown in **Figure 2.10** resulting in a periodic oscillation with a period described in **Equation 2-6**. This provides the possibility for the determination of the film thickness (T). In addition, considering a rough surface in the nanometer range, diffuse scattering can contribute to the scattered intensity. According to this, a roughness determination of both the film surface as well as the interface is also possible.

$$\Delta Q = \frac{2\pi}{T} \tag{2-6}$$

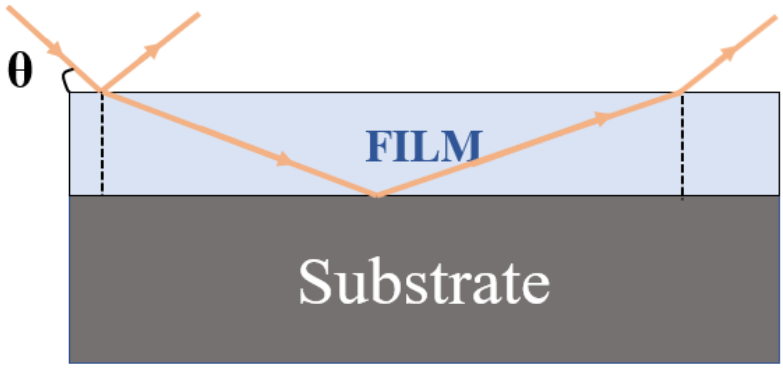

Figure 2.10 Sketch of the reflection at the film surface and the film-substrate interface.

3. Experimental Methods and Instruments

In this section, the growth and characterization methods as well as the corresponding instruments are shortly introduced. Thin films of $La_{0.7}Sr_{0.3}MnO_3$ are epitaxially grown by HOPSD. The physical properties of the as-prepared samples and the post-treated samples are characterized by various methods, i.e. XRD, XRR, AFM, SEM, NRA and SQUID magnetometry.

3.1 High Oxygen Pressure Sputter Deposition (HOPSD)

The sputtering technique is widely used in the field of thin film growth. In this thesis, the on-axis deposition from a stoichiometric target using high oxygen pressure sputter deposition (HOPSD, as shown in **Figure 3.1**) is employed to grow epitaxial $La_{0.7}Sr_{0.3}MnO_3$ thin film samples. The growth process can be described as follows: i) oxygen plasma generation using a 13.6 MHz radio frequency (RF, the maximum power is 200W), ii) Sputtering and ejection of the target atoms by bombardment of negatively charged oxygen ions originated from the oxygen plasma, iii) the ejected atoms or clusters move towards the substrate followed by surface diffusion, nucleation and growth.

Compared with the conventional low oxygen pressure deposition (in the range of 10^{-2} mbar or lower), HOPSD uses oxygen pressures in the range of 1 to 4 mbar and is more suitable to fabricate metal-oxides in a better quality. On the one hand, the large oxygen pressure can induce a lower mean free path (MFP) of oxygen ions due to the enhanced scattering with the background gas, thus resulting in a localization

of the oxygen plasma and suppressing the backscattering effect of the already deposited film [19]. Moreover, the above-mentioned effect depends not only on the oxygen pressure but on the target-substrate distance as well, in our study, a fixed value of 2 cm is used. On the other hand, the larger oxygen pressure can also ensure a lower oxygen vacancy concentration during the growth process.

In our HOPSD device, a two-stage pumping system is employed to achieve a vacuum in the range of 10^{-6} mbar. Then, oxygen gas is supplied by an oxygen cylinder and controlled through a mass flow controller (MFC) to achieve a desired oxygen pressure. The sample holder can be heated up to a maximum temperature of 1000 ℃ for the pre-treatment of the substrate as well as for enhancing the surface diffusion during the growth. In addition, targets with a diameter of 5 cm can be transported by a movable target arm and thus enable the choice of several materials for e.g. multilayer film growth.

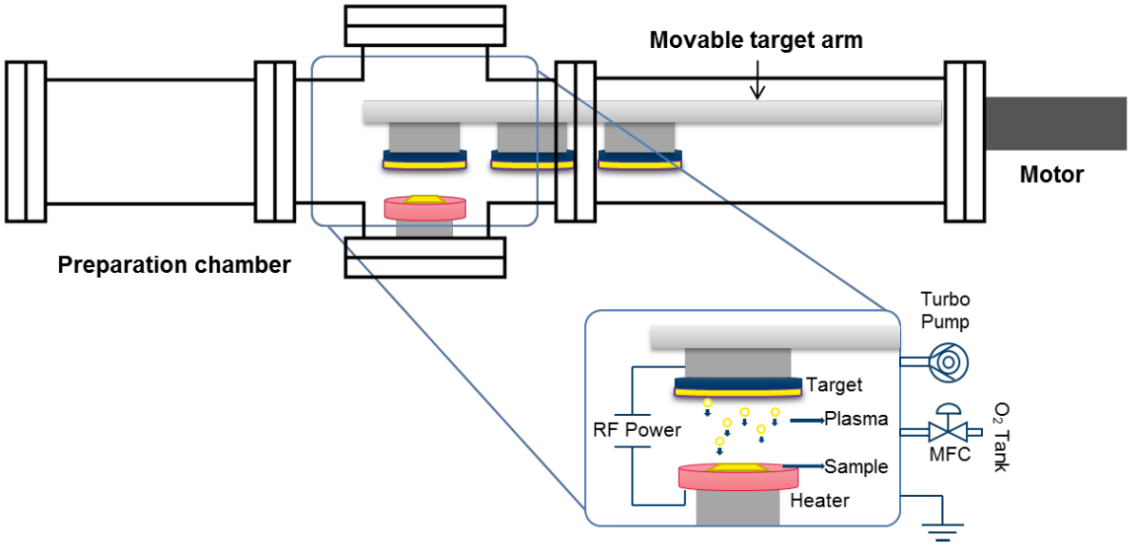

Figure 3.1 Sketch of the HOPSD device, figure taken from Ref [20]. On-axis RF sputtering with a maximum power of 200 W. The target-substrate distance is fixed at 2 cm.

3.2 X-Ray Reflectometry/ Diffractometry (XRR and XRD)

As shown in **Figure 3.2**, the D8 Advance X-ray reflectometer from Bruker AXS is employed to characterize the out-of-plane crystallinity as well as the thickness and the roughness of thin film samples. This device uses X-rays from the $Cu-K_{\alpha 1}$ characteristic line (1.54 Å), two Göbel mirrors are mounted in order to achieve a highly collimated beam for the reflectometry scan at lower angles, and a channel cut monochromator is installed for precise diffractometry scans at higher angles. In addition, a

vacuum chamber with a heating stage is installed to provide various sample environments (maximum vacuum: 1×10^{-6} mbar, maximum temperature: 750°C), which enable in-situ vacuum annealing. For powder samples, the crystal structure is characterized by a Huber Imaging Plate Guinier Camera G670 equipped with X-ray radiation from the $\mathrm{Cu} - \mathrm{K}_{\alpha}$ or $\mathrm{Mo} - \mathrm{K}_{\alpha}$ transition. By using a laser heating module and a closed-cycle cryostat, a sample environment in the high temperature range (673 K to 1773 K) or in the low temperature range (10 K to 300 K) can be realized.

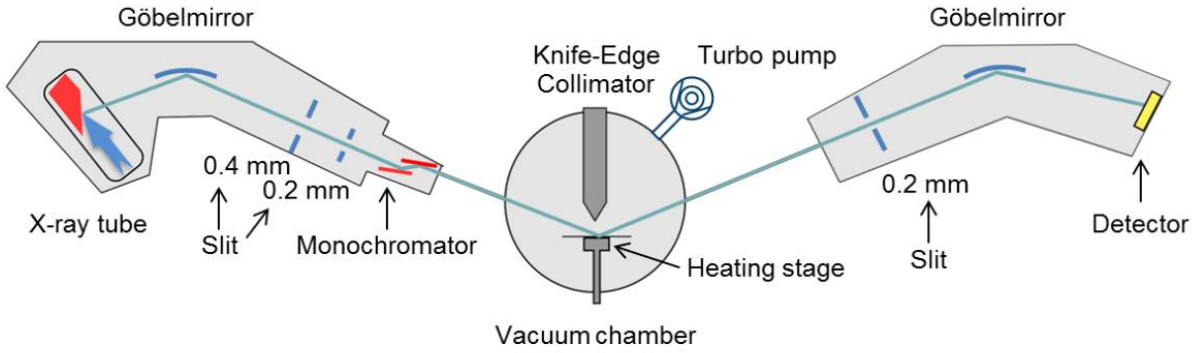

Figure 3.2 Sketch of the Bruker D8 Advance reflectometer equipped with a vacuum chamber and a heating stage, figure adopted from [21].

3.3 SQUID magnetometry (MPMS)

The Superconducting Quantum Interference Device (SQUID)-magnetometer from Quantum Design (model MPMS XL) with a sensitivity of 10^{-8} emu is employed to characterized the macroscopic magnetic properties of the thin film samples as well as of the powder samples. The basic principle of detection is illustrated in **Figure 3.3**. First, the thin film sample or powder pocket is mounted on a plateau created on the surface of a straw. Second, by moving up and down through the pick-up coils, the current induced by the magnetic moment of the sample can be transferred to the superconducting ring, and finally the response is measured with a LC-circuit.

Using the superconducting magnet, a magnetic field can be applied in the vertical direction with a maximum of 7 T. The sample environment temperature can be controlled between 1.9 K and 400 K. In addition, two measurement modes are usually adopted. For the direct current (DC) mode, the sample is moved through the pick-up coils in discrete steps. However, in the reciprocating sample option (RSO)

mode a harmonic oscillatory movement of the sample is used for a faster and low noise measurement.

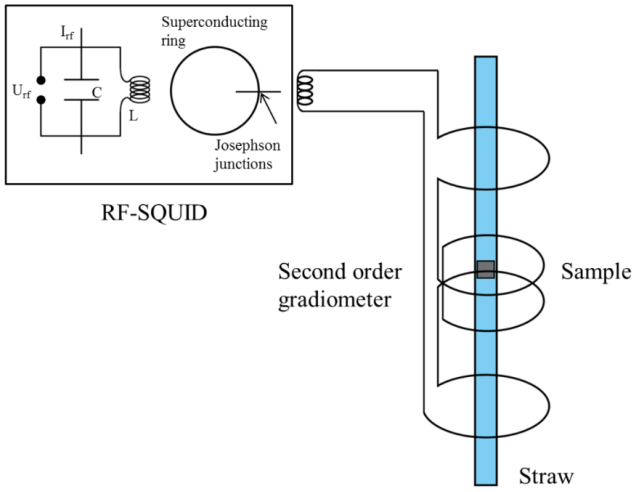

Figure 3.3 Sketch of the SQUID-magnetometer detection system, sample holder: straw with plateau, figure adopted from [22].

3.4 Atomic Force Microscopy (AFM)

The topographic information of thin film samples is collected by an Agilent 5400 atomic force microscope (AFM). The basic working principle is described in **Figure 3.4**. By using a laser diode as well as a photodetector, the deflection of the spring-like cantilever due to the tip-sample interaction is probed. Additionally, a feedback system equipped with a piezoelectric response element (this element can be arranged below the sample or combined with the cantilever) is used to calculate the signal from the photodetector and also to reposition the cantilever. Thus, a topography image can be obtained.

For AFM, three typical modes are introduced. First, when the feedback system is disengaged, there only exists the contact mode (static atomic force microscopy). Second, by driving the cantilever at a fixed frequency (near the intrinsic resonance frequency of the cantilever), a shift of the resonance frequency is induced by the tip-sample force (e.g. Van der Waals force), resulting in a change in the amplitude (dynamic atomic force microscopy). This change is recorded. Third, the intermittent contact mode or called tapping mode is adopted when driving the tip directly in a tapping fashion on top of the sample surface [23].

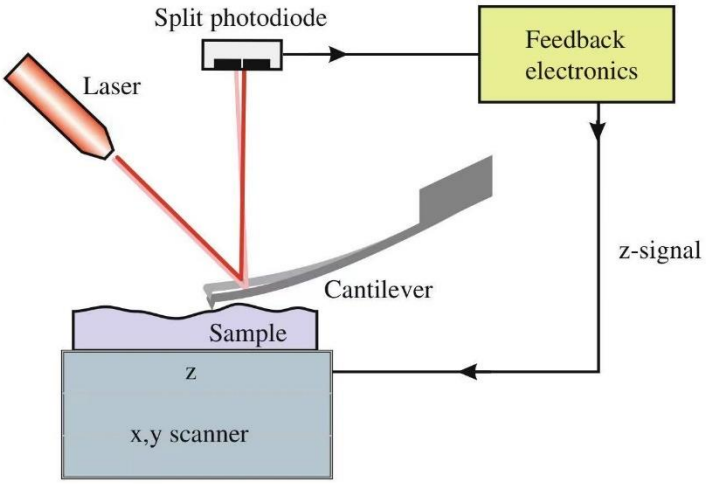

Figure 3.4 Schematic diagram of the AFM working principle, figure taken from [23].

3.5 Scanning Electron Microscopy (SEM)

The JSM-6510 Series scanning electron microscope (at the institute JCNS-1) is used to investigate the morphology of the powder samples. The schematic electron beam path is shown in **Figure 3.5**. When illuminating the sample surface with the electron beam, various signals can be exited i.e. Secondary electrons (SEs), backscattered electrons (BSEs), and Auger-electrons (AEs). The SEs originated from inelastic scattering between electron beam and the sample surface are usually collected as the signal for topographic analysis, while the BSEs being produced by elastic collisions in deeper regions are used for chemical composition contrast imaging [24].

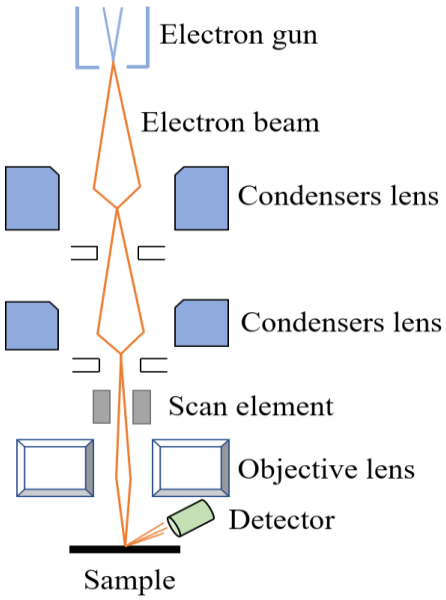

Figure 3.5 Schematic diagram of an SEM microscope.

3.6 Nuclear Reaction Analysis (NRA)

Using nuclear reaction analysis (NRA) the hydrogen content in the thin films is probed. The sketch of the NRA process is illustrated in **Figure 3.6**. When the thin film sample is irradiated with MeV ion beams (e.g. ^{15}N or ^{19}F), a nuclear reaction described in **Equation 3-1** can be triggered under the resonance condition. By measuring the yield of emitted characteristic gamma-rays, the hydrogen content is quantified [25, 26].

$$^{15}N + {}^{1}H \rightarrow {}^{12}C + \alpha + \gamma(4.43MeV) \quad (3\text{-}1)$$

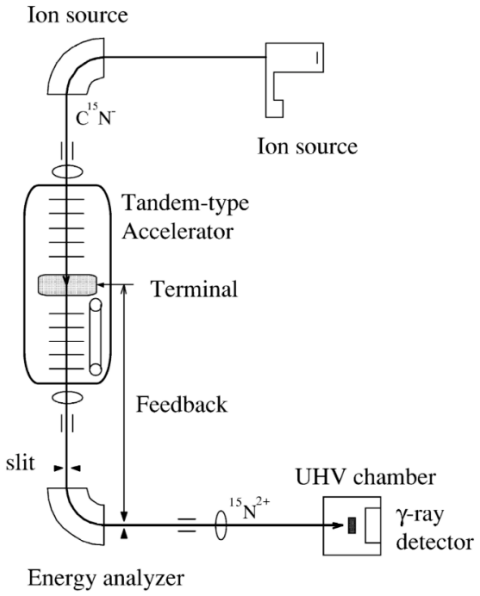

Figure 3.6 Sketch of the NRA process, figure taken from [26].

4. Control of physical properties via ionic liquid gating on LSMO thin films

4.1 Ionic liquid gating method and experimental configuration

By applying a voltage using an ionic liquid, which consists of organic electrolytes $[\mathrm{DEME}]^{+}[\mathrm{TFSI}]^{-}$, various physicochemical phenomena can be triggered. The anions and cations inside the ionic liquid will be driven by an electric field and accumulate at the corresponding electrode. The accumulated charge will also induce an accumulation of opposite charge at the solid side by electrostatic induction, thus forming an electric double layer (EDL, illustrated in **Figure 4.1**) with a thickness of several

nanometer (much smaller than the film thickness involved in this thesis). This induces a large electric field near the solid surface. Moreover, the charge accumulation at the inner surface of the solid can introduce charge depletion in the rest of the film solid, thus enabling electrostatic doping [27]. Such electrostatic doping can trigger the change of orbital occupancies and tune the magnetic properties [28].

Second, by a higher gating voltage the insertion or removal of ions as well as electrochemical reactions can be induced. As described in **Equation 4-1**, this potential electrochemical reaction will introduce oxygen vacancies inside the film [29]. When exposing the ionic liquid to air, traces of water moisture will be introduced. This can contribute both as a source of hydrogen for insertion (i.e. hydrogen ions are small enough to enter the LSMO lattice) or can promote electrochemical reactions. Such so-called dual ionic-transfer (hydrogen and oxygen) has been demonstrated through ionic liquid gating recently [30].

$$La_{0.7}Sr_{0.3}[Mn_{0.7}^{3+}Mn_{0.3}^{4+}]O_3 + 2\delta e^- + \delta H_2O \leftrightarrow$$
$$La_{0.7}Sr_{0.3}\left[Mn_x^{2+}Mn_{2\delta-x}^{3+}Mn_{0.7-x}^{3+}Mn_{0.3-(2\delta-x)}^{4+}\right]O_{3-\delta} + 2\delta OH^- \quad (4\text{-}1)$$

The experimental configuration is shown in **Figure 4.1.** The voltage is supplied by a Model 2400 Source-Meter through platinum wires with a diameter of 50 μm. The platinum wires are fixed by conducting Acheson Silver DAG 1415M glue at the four corners of the LSMO thin film surface, thus enabling the entire LSMO thin film (size: 5 mm × 5 mm) as the cathode. Similarly, a platinum sheet with the same area as the LSMO thin film is also connected by a platinum wire at the surface center and acts as the anode. The cathode and anode are separated horizontally by ca. 2 mm and are both surrounded by sufficient ionic liquid.

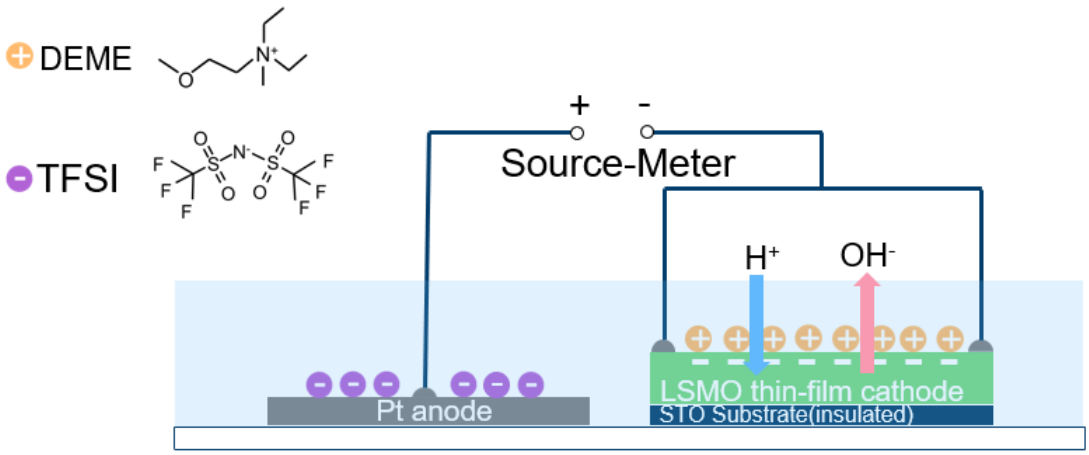

Figure 4.1 Ionic liquid gating experimental configuration.

4.2 Film growth and ionic liquid gating parameters

For the LSMO film growth by HOPSD, $SrTiO_3$ (STO) substrates with (001) orientation from Crystec or Shinkosha company are selected. As illustrated in **Figure 4.2 (a)**, among other perovskite substrates, STO as well as $(LaAlO_3)_{0.3}(Sr_2AlTaO_6)_{0.7}$ (LSAT) shows a lattice mismatch smaller than 1 %, which fits well the requirement for the epitaxial growth [31]. Compared with LSAT, the STO has a simpler chemical composition and also exhibits a lower risk for interdiffusion. Moreover, according to **Figure 4.2 (b)** the small thermal expansion coefficient as well as the good structural stability (cubic) between the room temperature and the growth temperature (>800 K) makes STO the best candidate for LSMO growth.

Apart from the substrate, the growth temperature, oxygen pressure, plasma power, and the growth time determine the film quality. Before the formal sputtering, a pre-sputtering procedure is used to remove the adatoms on the target. In the meantime, the substrate is annealed at 950 °C to achieve an atomically-flat surface [32]. As shown in **Table 4.1**, LSMO thin films involved in the **chapter 4** are all grown at the same optimized parameters [33]. After growth, the samples SP561 and SP568 are divided into 4 segments, labeled by -1, -2, -3, and -4, respectively. Correspondingly, the gating parameters for samples SP561-3, SP565, SP568-2, and SP568-4 are shown in **Table 4.2**.

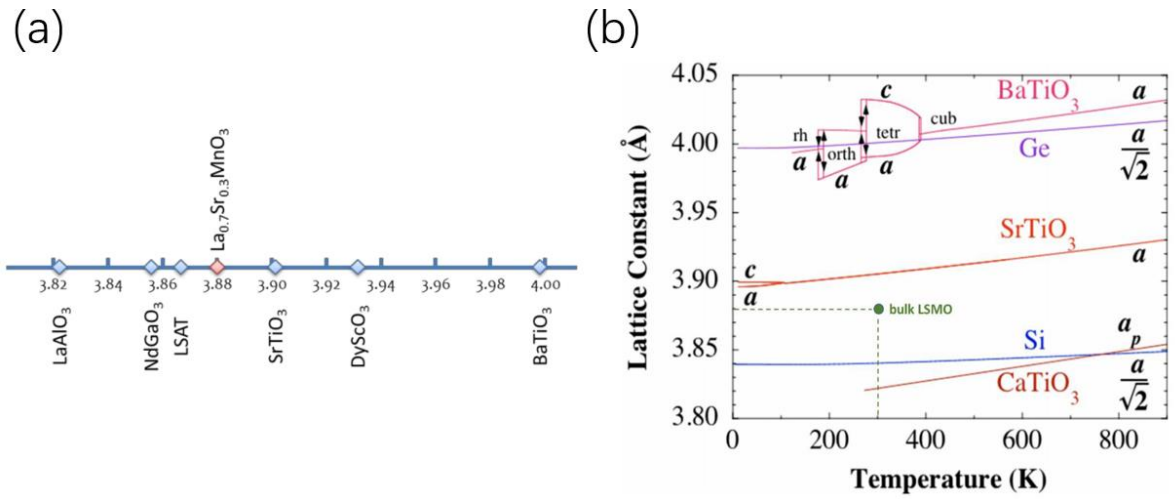

Figure 4.2 (a) Lattice parameter of perovskite substrates at room temperature, figure adopted from [4]. (b) Temperature dependence of the perovskite substrate structure, figure taken from [34].

Table 4.1 Substrate information and growth parameters.

Sample ID	Substrate size [mm x mm]	Substrate company	Growth temperature [°C]	Oxygen pressure [mbar]	Plasma power [W]	Growth time [min]
SP561	10 x 10	Shinkosha	800	2	120	60
SP565	5 x 5	Crystec	800	2	120	60
SP568	10 x 10	Shinkosha	800	2	120	60
SP572	5 x 5	Crystec	800	2	120	60

Table 4.2 Ionic liquid gating parameters.

Sample ID	Gating Experiment Stage 1		Gating Experiment Stage 2	
	Voltage [volt]	Time[min]	Voltage[volt]	Time[min]
SP561-3	4	45	0	0
SP565	5	30	0	0
SP568-2	5	120	0	0
SP568-4	5	60	6	10

4.3 Changes of physical properties after ionic liquid gating

In this section the influence of ionic liquid gating at various parameters onto the physical properties of LSMO thin films will be discussed.

4.3.1 Topographical changes (AFM)

The topographical changes before (as-prepared state of SP572) and after ionic liquid gating (gated state of SP565, 5V 30min gating) are characterized by atomic force microscopy. For the as-prepared state of SP572, the data is collected from SP572 after HOPSD growth which has the same growth parameters as all the other three samples for gating. For the gated state of SP565, the AFM is measured after 5min ultrasonic cleaning to remove the attached ionic liquid and contamination.

Figure 4.3 shows the AFM image of both the as-prepared and gated state. The results indicate that the surface of the as-prepared state shows a good uniformity and a mean roughness of 2.5 nm. However, for the gated state, obvious dots and islands with a maximum height of 30 nm emerge, indicating the destruction of the film surface. One might assume that the gated film is partially decomposed by a large oxygen vacancy formation under this gating voltage (5V). Since the surface of gated state film is no longer homogeneous further resistivity measurements are not performed.

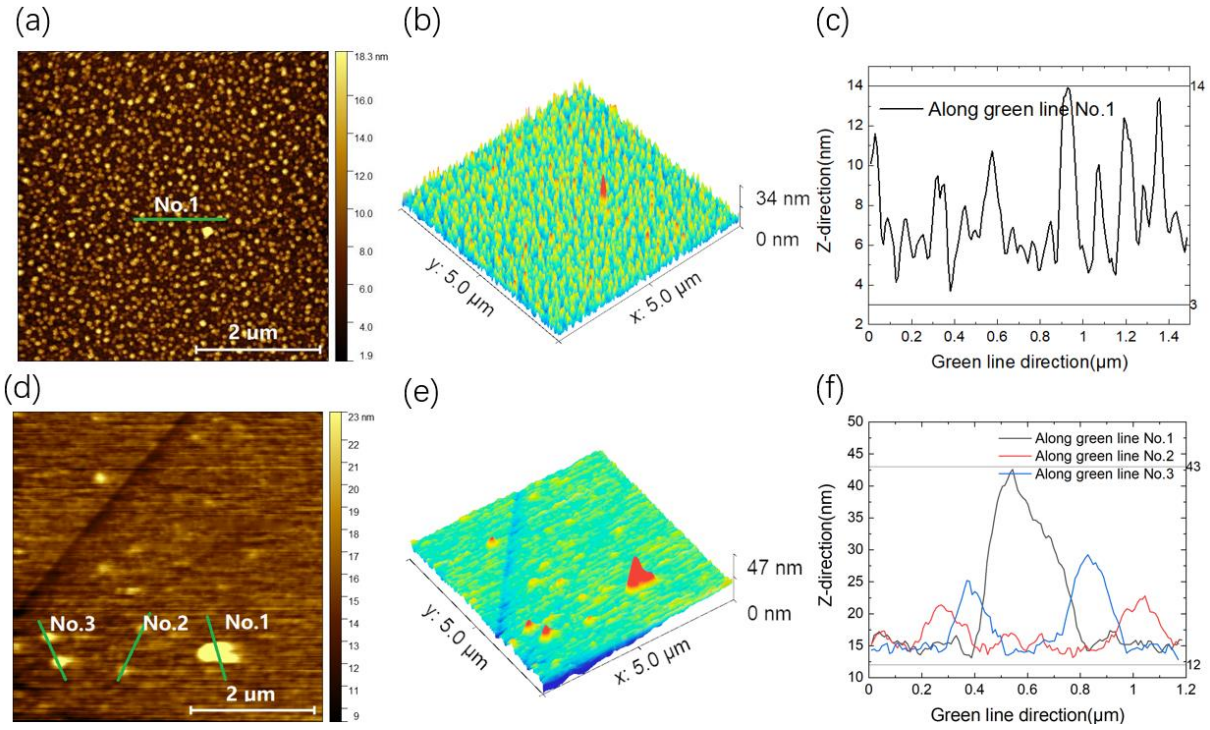

Figure 4.3 AFM measurements of as-prepared and gated state. Panel (a), (b), and (c) show the 2D, 3D, and height variation profile along a particular direction (green line No.1), respectively, of the as-prepared state of SP572. Panel (d), (e), and (f) show the 2D, 3D, and height variation profile along a particular direction (green line No.1, 2 ,3) of the gated state of SP565 (5V 30min gating).

4.3.2 Structural changes (XRD and XRR)

In this subsection, the XRD and XRR spectra before and after ionic liquid gating are shown. **Figure 4.4** and **Figure 4.5** show the corresponding XRD and XRR spectra of the four as-prepared samples involved in the **chapter 4**. The calculated out-of-plane lattice parameter by using Bragg equation as well as the thin film thickness and roughness derived from XRR using software Gen X are shown in **Table 4.3**. First, the XRD spectrum shows for all the samples almost the same shape of the LSMO (002) Bragg peak, that indicates the HOPSD instrument has an overall good repeatability of thin film growth. Besides that, the reduced out-of-plane parameter 3.85 Å implies the tensile strain induced by the STO substrate in the in-plane direction. In addition, the sharp LSMO (002) peak and the clear oscillations demonstrate that all the samples have a good crystal quality. Second, by fitting the XRR spectrum one can conclude that all the sample exhibit a thickness around 40 nm, a roughness of 2 to 3 nm (this roughness also confirmed by AFM), and a scattering length density (SLD) between 4.82×10^{-5} Å^{-2} and 4.59×10^{-5} Å^{-2}. Moreover, the substrates from different companies do not show an obvious influence on the sample growth.

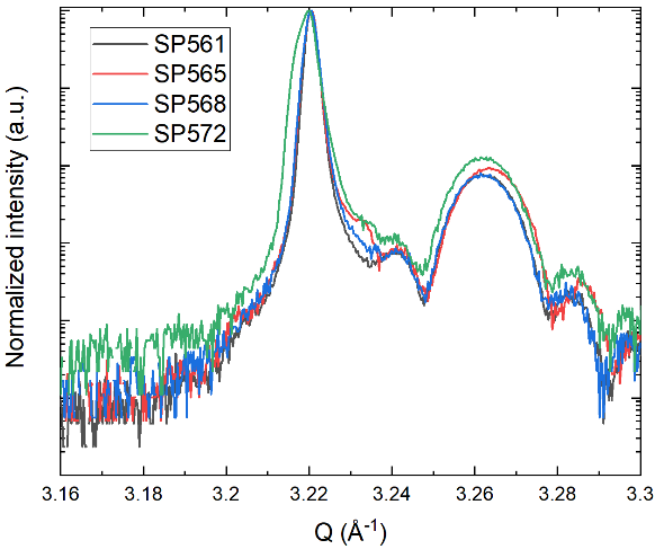

Figure 4.4 XRD spectrum of as-prepared state of SP561, SP565, SP568, and SP572 before the gating experiment.

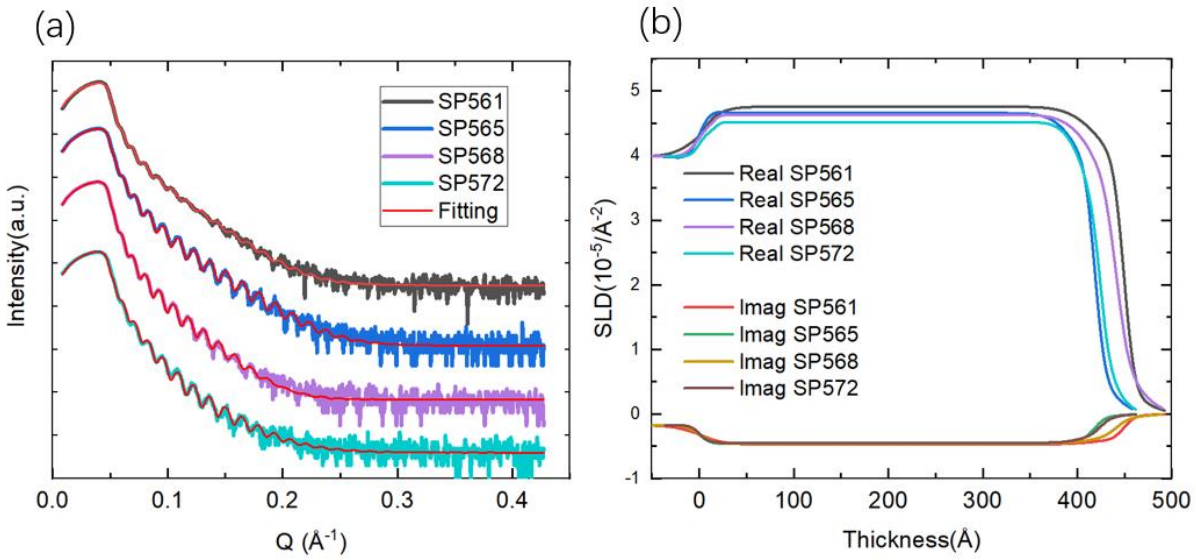

Figure 4.5 (a) Fitted XRR spectrum of the as-prepared state of SP561, SP565, SP568, and SP572 before gating experiment. (b) Fitted scattering length density (SLD).

Table 4.3 Results fitted using XRD and XRR spectra of SP561, SP565, SP568, and SP572.

Sample ID	**Out of plane lattice parameter [Å]**	**LSMO thickness [Å]**	**LSMO roughness [Å]**	**Scattering length density [$Å^{-2}$]**
SP561	3.852 $\pm(7.17\times10^{-4})$	428.76 $\pm(7.24\times10^{-2})$	30.97 $\pm(4.16\times10^{-2})$	4.82×10^{-5} $\pm(3.38\times10^{-9})$
SP565	3.850 $\pm(6.76\times10^{-4})$	413.49 $\pm(2.87\times10^{-3})$	25.83 $\pm(4.66\times10^{-3})$	4.73×10^{-5} $\pm(3.35\times10^{-10})$
SP568	3.852 $\pm(9.59\times10^{-4})$	419.91 $\pm(1.91\times10^{-4})$	30.00 $\pm(3.68\times10^{-5})$	4.71×10^{-5} $\pm(3.33\times10^{-11})$
SP572	3.852 $\pm(1.37\times10^{-3})$	402.47 $\pm(3.37\times10^{-1})$	21.60 $\pm(6.78\times10^{-2})$	4.59×10^{-5} $\pm(8.90\times10^{-8})$

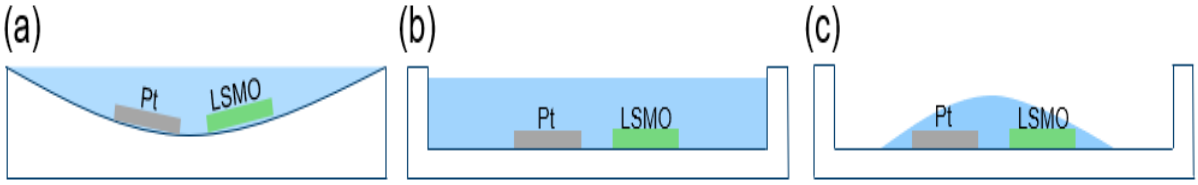

Figure 4.6 Sketch of the ionic liquid gating reaction cell. (a) Plastic reaction cell for SP561 and SP565. (b) Quartz reaction cell for SP568-2. (c) Quartz reaction cell with less ionic liquid (blue) for SP568-4.

Figure 4.6 shows the sketches of reaction cells for each gating experiment. **Figure 4.7** shows the XRD spectrum after ionic liquid gating. By comparing as-prepared state and SP561 gated state (4V 45min gated), no obvious peak shift can be found (**Figure 4.7 (a)**). This might indicate that a voltage threshold is needed for triggering the ion insertion as well as the electrochemical reaction. Then the voltage is increased to 5V, with shorter gating time (30min), one finds that the LSMO (002) Bragg peak shifted to the left side of the (002) Bragg peak of the STO substrate and formed an extended plateau. This might indicate the lattice expansion due to a larger ionic radius of the Mn at lower valences, which could be triggered by the formation of the oxygen vacancies or the insertion of hydrogen. The plateau formation might be due to the fact that the films are not transformed homogeneously, thus introducing a broad distribution of different areas with different states and contributing Bragg peaks at a distribution of different angles.

As in **Figure 4.7 (c)** shown, when increasing the gating time from 30min (SP565) to 120min (SP568-2) under the same voltage (5V), surprisingly, the plateau will not significantly further extend (more clear comparison between **Figure 4.7 (b)** and **(d)**), and also without obvious decrease of the plateau peak intensity. It indicates that the gating effect terminated at a certain point. This phenomenon could be explained by a self-passivation region.

On the one hand, at the beginning of gating, regions near the silver glue (silver glue at the film four corners for electrical contacts) will first of all be transformed and the resulting lattice expansion will suppress double exchange and increase resistivity. After these surrounding areas become insulating, there is no possibility for the further transformation of the center part in the thin film which contributes to the most XRD signal. On the other hand, with increasing formation of oxygen vacancies, the LSMO

thin film will laterally fragment into islands (partial decomposition, as shown in **Figure 4.3**), which are isolated from each other and thus avoid further transformation.

Moreover, the gating voltage is further increased to 6V. Compared with the SP568-2 (5V 120min gated), with shorter gating time and less ionic liquid, the SP568-4 (60min + 6V 10min gated) show a further plateau expansion. This small additional transformation can be attributed to the higher voltage.

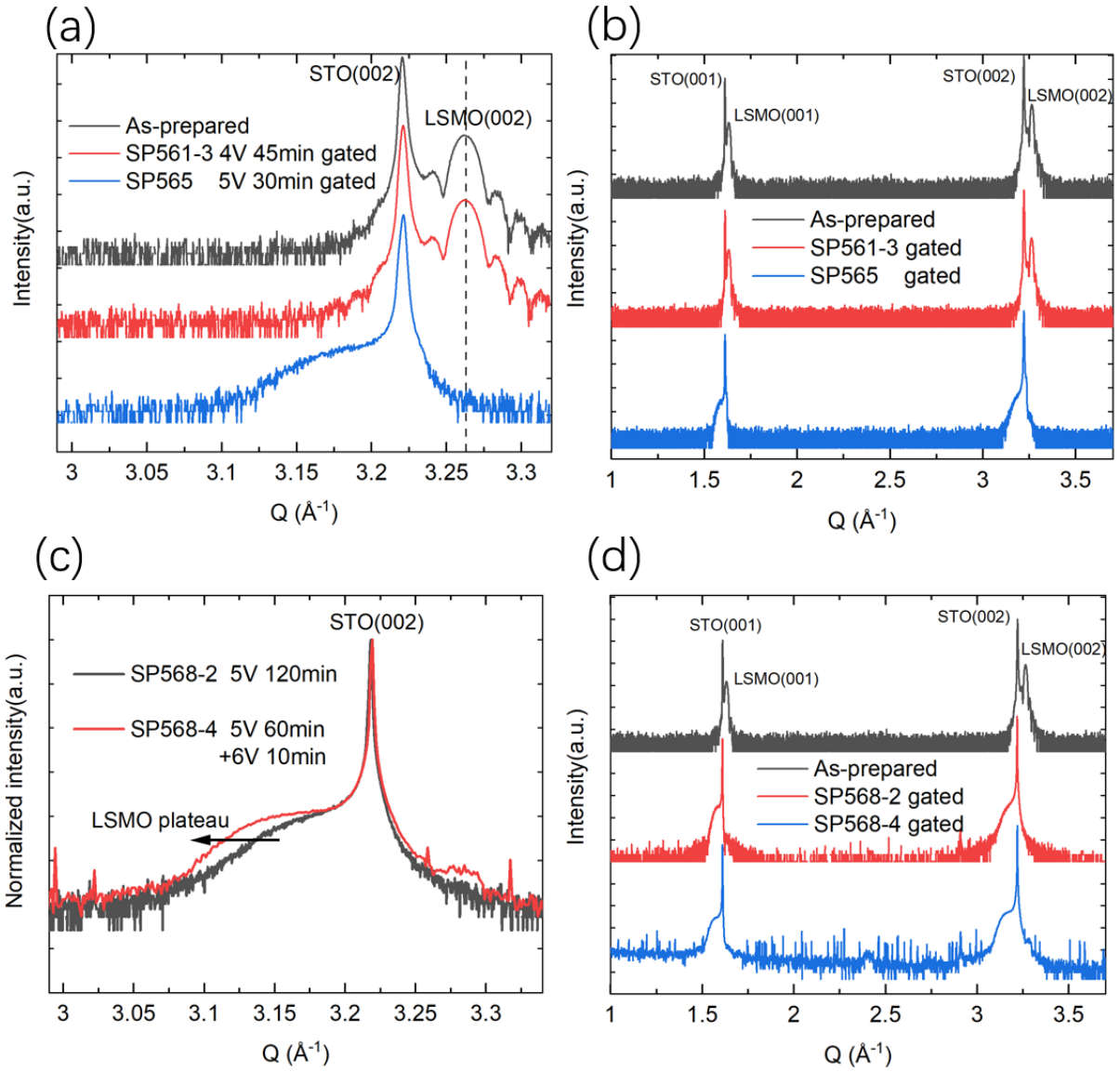

Figure 4.7 XRD spectrum after gating. (a) As-prepared state, 4V 45min gated SP561, and 5V 30min gated SP565. (b) Broader scan range of (a). (c) 5V 120min gated SP568-2, 5V 60min+6V 10min gated SP568-4. (d) Broader scan range of (c).

In **Figure 4.8 (a)**, the areas covered by the silver glue during the gating experiment show a darker color, this is the typical signature of as-prepared perovskite state. These untransformed areas will also

introduce a signal under grazing incidence, which leads to the complicated XRR spectrum as shown in **Figure 4.8 (b)**. Given the above observations, the thickness calculation for the gated film by XRR fitting is hence not accurate.

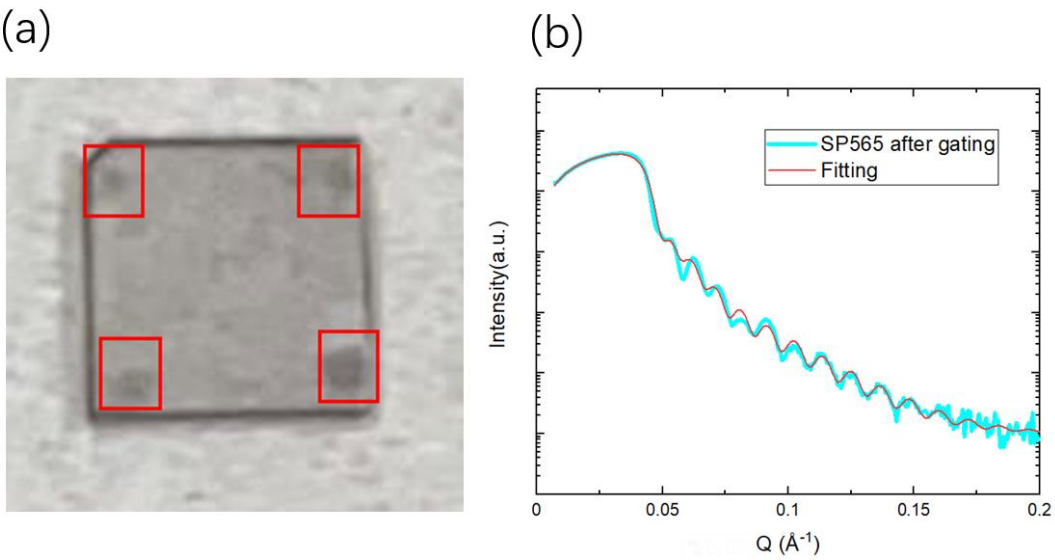

Figure 4.8 (a) Image of the gated sample SP568-4, the areas in the red box which show darker color stay unchanged due to the coverage of silver glue. Here SP568-4 is shown rather than SP565 due to the lighter color of the Shinkosha substrate and thus a better contrast. (b) Unsuccessful fitting of the gated SP565 XRR spectrum due to the complicated signal introduced by the untransformed region at the corners.

4.3.3 Changes of magnetic behavior

To study the influence of ionic liquid gating on film magnetic property, the magnetic behavior of the two gated samples i.e., SP565 and SP568-4 are characterized by SQUID magnetometry. **Figure 4.9 (a)** shows the hysteresis loops of the as-prepared and the gated sample measured at 10K. For all the sample, the rectangular shaped loops indicate that the magnetization reversal occurs by domain wall motion. In addition, the saturated hysteretic behavior above 1000 Oe corresponds to a typical ferromagnetic material signature [35]. The as-prepared state shows a saturation magnetization (M_S) of 3.45 μ_B/Mn, which is lower than the bulk value 3.7 μ_B/Mn [36]. This might due to the influence of interface and strain in the thin film system. When ionic liquid gating is introduced, one can observe a significant decrease of M_S as well as an increase of coercive field (H_c). At higher gating voltages, this effect is enhanced. Frist, one might assume that the lower Mn valences induced by hydrogen insertion or oxygen vacancy formation as well as the corresponding lattice expansion can suppress the double exchange between Mn^{3+} and Mn^{4+} and resulting in a reduced M_S. Moreover, the decomposition introduced

by gating can also contribute to the decrease of M_S. Second, defects introduced by ionic liquid gating (inserted hydrogen or oxygen vacancy) can pin the domain wall motion and induce a larger H_C.

Figure 4.9 (b) shows field cooling (FC) curves measure at 100 Oe. In the FC curve, the as-prepared state shows the typical ferromagnetic behavior with a Curie temperature (T_C) around 325 K. Moreover, one finds that there is a strong decrease of magnetization after gating as well, which can also be explained by suppression of double exchange. In addition, the lower T_C with a smearing-out shape corresponds to the weaker double exchange and an inhomogeneous system. The kink around 105 K might induced by the cubic-to-tetragonal phase transition of STO substrate as shown in **Figure 4.2 (b)**.

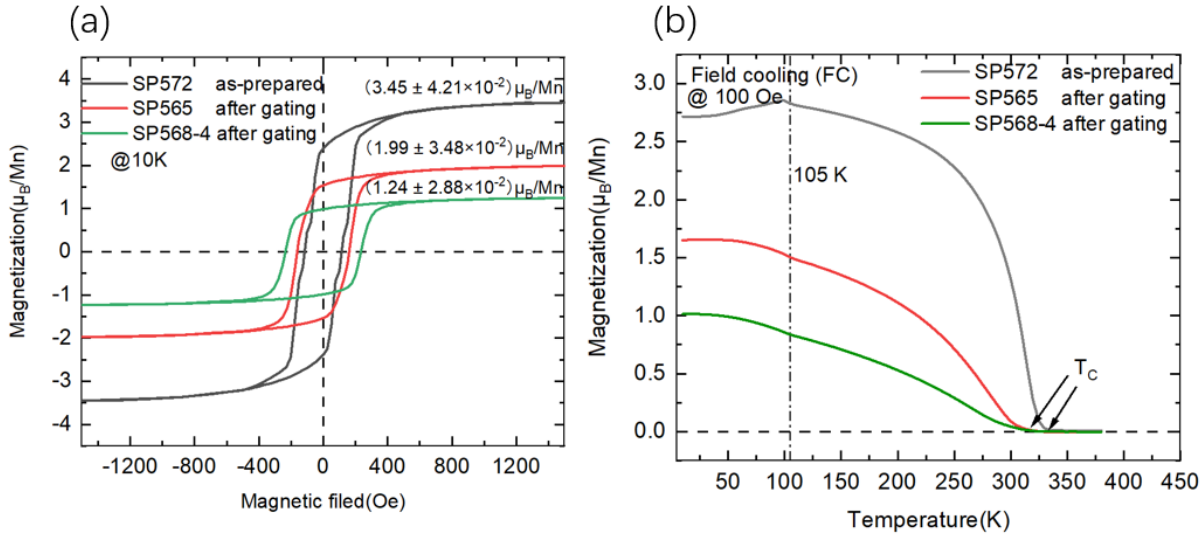

Figure 4.9 (a) Normalized hysteresis loops of the as-prepared samples, i.e. SP572 and the gated samples, i.e. SP565 and SP568-4. The normalization is based on the corresponding as-prepared state of each sample. (b) Corresponding field cooling curves measured at 100 Oe.

4.3.4 Changes in hydrogen content

Figure 4.10 shows the hydrogen content depth profile of gated sample (i.e. SP565 and SP568-4) measured by nuclear reaction analysis (NRA) at HZDR Dresden by Lei Cao. The data is collected beyond the depth of 20 nm in order to eliminate the influence of surface adsorbed water. The hydrogen content in the films has two possible origins. On the one hand, hydrogen originated from water splitting can be inserted into the film by the electric field applied through the ionic liquid [30]. On the other hand, the electrochemical reaction can also provide hydroxides which might partially remain in the film. For both gated samples, a large hydrogen content (20% and 30%) is found near the film surface and monotonically decrease with increasing depth. The sample (SP568-4) treated by a higher gating voltage

shows an overall higher hydrogen content. The results might suggest that with higher gating voltage the enhanced hydrogen insertion as well as more remanent hydroxide produced by the electrochemical reaction can be triggered. Moreover, the higher hydrogen content of SP568-4 compared with SP565 corresponds well with the more extended plateau in XRD spectrum as well as more reduced M_S in the hysteresis loop.

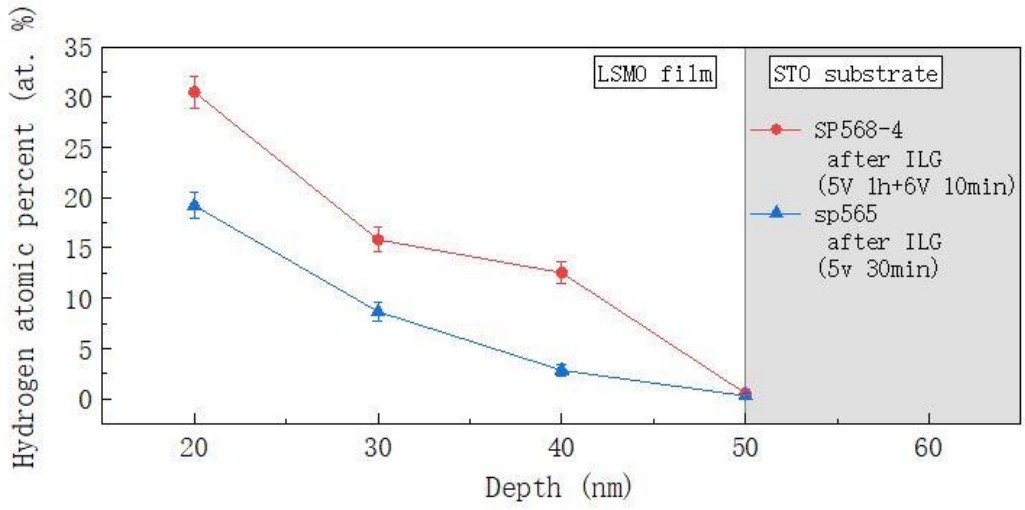

Figure 4.10 Hydrogen content depth profile of LSMO thin films after ILG measured at HZDR by Dr. Lei Cao.

4.4 Summary

Employing a systematic study of ionic liquid gating, one could conclude that after ionic liquid gating, the hydrogen insertion triggered by electric field (as shown in **chapter 4.3.4**) as well as the oxygen vacancy introduced by potential electrochemical reaction can lower the valence of Mn ions and thus inducing an inhomogeneous lattice expansion (as shown in **chapter 4.3.2**). This will lead to a decreased magnetization and a lower T_c (as shown in **chapter 4.3.3**). Furthermore, the gating effect is terminated by a self-passivation process. Nevertheless, ionic liquid gating can exhibit a strong effect onto LSMO films and tune its physical properties.

5. Control of physical properties via topotactic phase transition on LSMO powders by post-annealing

5.1 Powder sample preparation

The powder sample of LSMO is prepared by hand milling using an old target from the HOSPD system. Thus, the LSMO thin film and the LSMO powder in this thesis should approximately share the same stoichiometry. The old target was firstly polished by P400 sand paper to remove the bonded metal, then treated by iso-proposal to clean attached contamination particles. After that, 30min hand milling was conducted inside a SiO_2 crucible. Through the above-mentioned preparation method, two as-prepared powder samples are produced, named R1 and R2. Scanning electron microscopy (SEM) is used to characterize the morphology and grain size of the as-prepared powder samples.

Figure 5.1shows the SEM images of the two as-prepared LSMO powder samples, R1 and R2. On the one hand, from the overall morphology image (**Figure 5.1 (a)** and **(d)**), one can see that for both samples the grain size has a broad size distribution (from 0.1μm to 100μm) as expected for hand-milled powders. The composition contrast (**Figure 5.1 (b)** and **(e)**) confirms a good composition uniformity and no contamination. The local morphology images (**Figure 5.1 (c)** and **(f)**) indicate that the two as-prepared samples have the similar average grain size of approximately 5 nm.

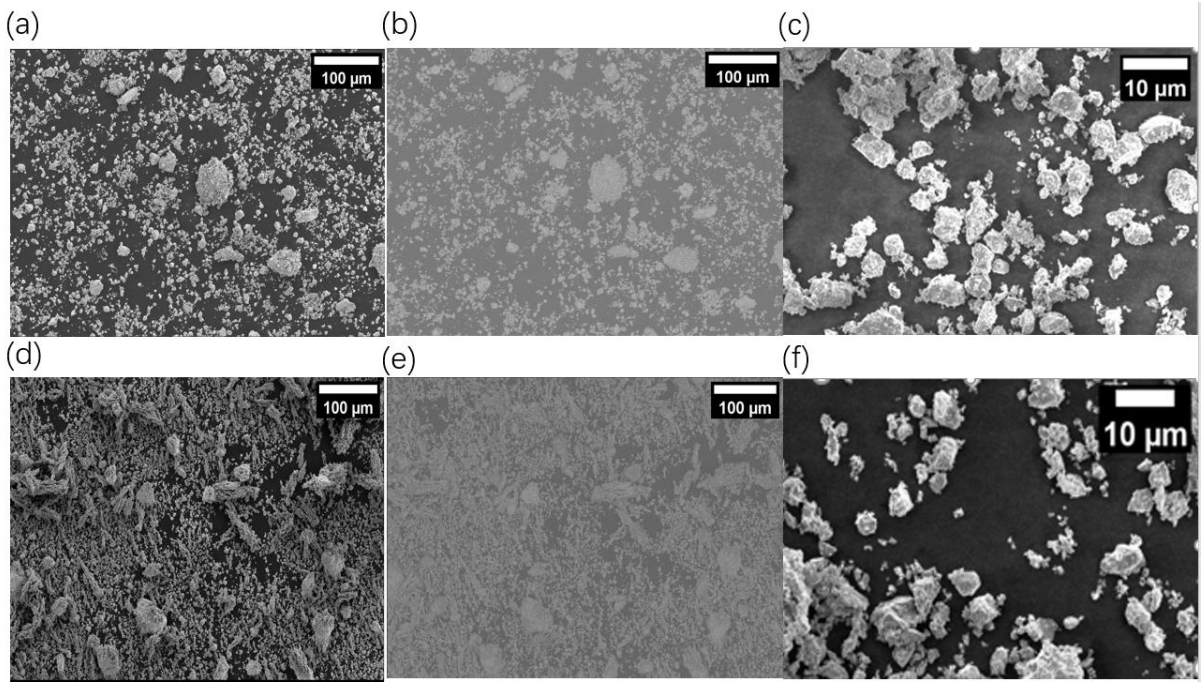

Figure 5.1 SEM images of the as-prepared powder samples. Panels (a), (b), and (c) show the overall morphology, overall composition contrast, and local morphology, respectively, of the as-prepared sample R1. Panels (d), (e), and (f) show the overall morphology, the overall composition contrast, and local morphology, respectively, of the as-prepared sample R2.

5.2 Topotactic phase transition induced by aluminum-assisted annealing

In this subsection, the experiments of Aluminum-assisted vacuum annealing will be explained and the influence introduced by the oxygen vacancy triggered topotactic phase transition onto the physical properties will be discussed.

5.2.1 Experimental configuration

As shown in **Figure 5.2**, the as-prepared LSMO powder is sealed with freshly polished Aluminum-foil as oxygen getter in the quartz tube with a length of 15 cm and a diameter of 2 cm. Two types of sandpaper for Al polishing are used in this annealing experiment, i.e. P280 and P400.The sealing of the quartz tube can be conducted in a vacuum of 10^{-5} mbar (standard sealing vacuum) or under specific request (pumping longer, i.e., overnight or over weekend) in the range of 10^{-6} mbar. Further, the sealed vacuum tubes are heated in a furnace under various temperatures and for various times to trigger the topotactic phase transition.

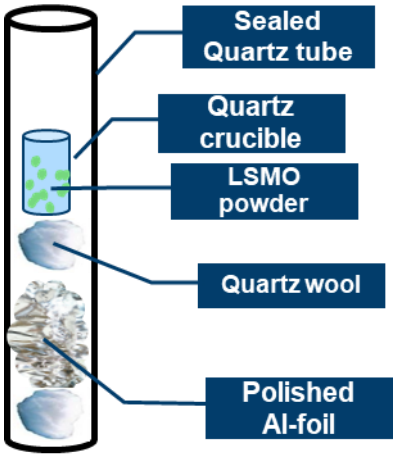

Figure 5.2 Sketch for Aluminum-assisted vacuum annealing in a quartz crucible.

5.2.2 Aluminum-assisted annealing for the as-prepared sample R1

In this subchapter, the annealing experiments are based on the as-prepared sample R1. Here aluminum foil is polished by sand paper P280 and sealed under standard vacuum conditions, i.e. 10^{-5} mbar. Each annealing experiment is independent of each other.

5.2.2.1 Annealing condition dependent structural changes

In this set of annealing experiments, the annealing time was fixed at a sufficiently large value i.e.75h. In order to study the influence of annealing temperature onto the topotactic phase transition, temperatures of 650°C, 600°C, and 550°C are used. The corresponding XRD spectrum is shown in **Figure 5.3**. First, the as-prepared sample R1 shows typical perovskite (PV) structure which indicates a good crystal quality. When annealed at highest temperature 650°C, which is near the melting point of aluminum (660°C), the structure of the LSMO powder stays almost unchanged, indicating that the aluminum does not exhibit obvious oxygen absorption. Considering this result, the annealing temperature is reduced. With a decreased temperature one can observe a structural variation starting from 600°C and below. At 600°C, the intensity of some perovskite Bragg peaks decrease (blue arrows). At 550°C the XRD spectrum shows several new emerged Bragg peaks (green arrows). This suggests the formation of an intermediate state. At this vacuum condition of 10^{-5} mbar and in this set of annealing experiments the brownmillerite (BM) structure cannot be achieved.

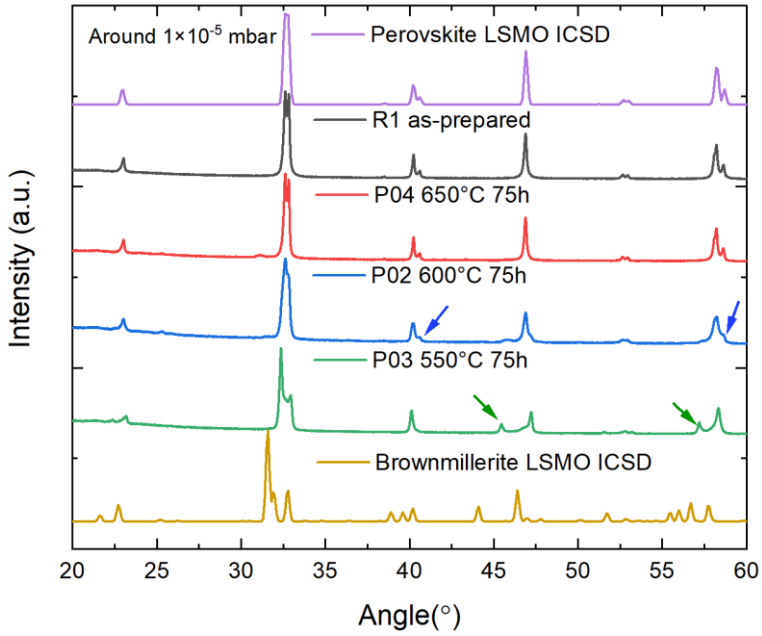

Figure 5.3 XRD spectrum of the as-prepared sample R1and samples annealed at different temperatures with the same time. The blue arrows show the decreased Bragg peaks of the 600°C and 75h annealed sample. The green arrows show the newly emerged Bragg peaks of the 550°C 75h annealed sample.

5.2.2.2 Magnetometry measurements

Using SQUID magnetometry, the magnetic properties of the as-prepared powder sample R1 and the annealed powder samples are characterized. The magnetization is normalized to mass. **Figure 5.4** shows the normalized hysteresis loops of the as-prepared and annealed samples, all the samples show a S-

shape loop which indicates a magnetization reversal by incoherent rotation which is typical for powder samples. When decreasing the annealing temperature, with the emerging of the intermediate state (as mentioned in the **chapter 5.2.2.1**), a significant decrease of magnetization from the field cooling (FC) curve (**Figure 5.5 (b)**) is observed. Moreover, by normalization of the magnetization to the value at 350K, where the anti-ferromagnetic contribution can be regarded as negligible, the remanent ferromagnetic contribution can be calculated. For the intermediate state formed in the 550°C for 75h annealed sample, only 2.8 % ferromagnetic contribution can be found. From the zero-field cooling (ZFC) curve (**Figure 5.5 (a)**), the intermediate state shows a typical anti-ferromagnetic behavior with a Néel-temperature around 55K.

These results can be explained that the aluminum-assisted vacuum annealing can transform the lattice structure by formation of oxygen vacancies. The oxygen vacancies decrease the oxidation state of manganese. The manganese ion with decreased oxidation state can introduce a lattice expansion and thus suppress the double exchange mechanism between Mn^{4+} and Mn^{3+}. The super-exchange interaction will then dominate when there exits sufficient Mn in lower valence states and that will lead to antiferromagnetic behavior [4].

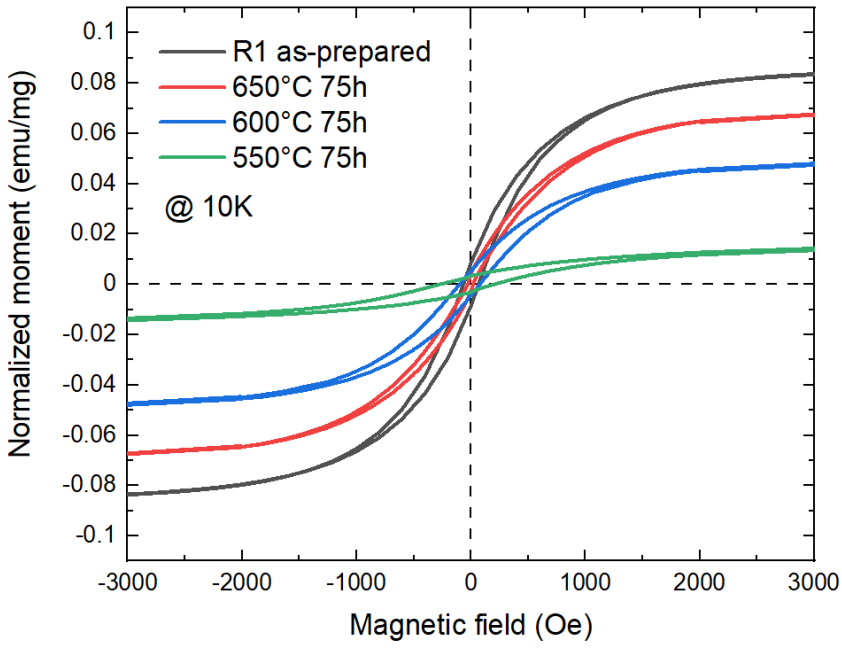

Figure 5.4 Normalized hysteresis loops of the as-prepared samples and the annealed samples, measured at 10K.

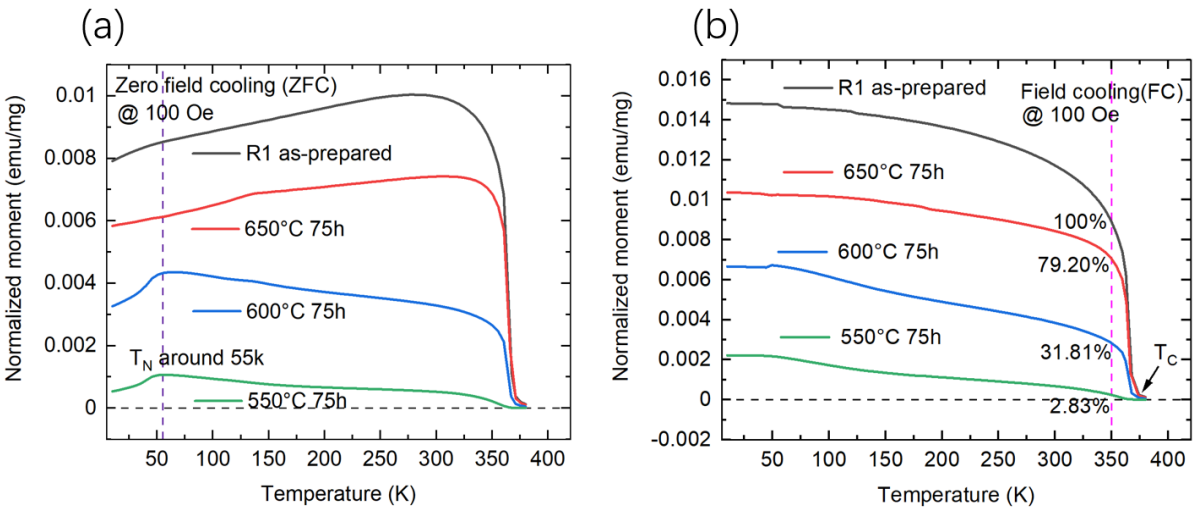

Figure 5.5 Magnetization-temperature curve of the as-prepared powder sample R1 and the annealed samples measured at 100 Oe. Panel (a) shows the zero-field cooling (ZFC) curve. Panel (b) shows the field cooling (FC) curve.

5.2.3 Aluminum-assisted annealing for the as-prepared sample R2

In this subsection, the aluminum-assisted annealing experiments are based on the as-prepared sample R2 and aluminum foil with the standard size $5\ \text{cm} \times 13\ \text{cm}$ (mass around 0.55 g) polished with finer sand paper P400. In each tube the LSMO powder samples are loaded with an amount of 0. 05 g. Then the quartz tube is sealed at a better vacuum in the range of 10^{-6} mbar. Each annealing experiment is independent of each other.

5.2.3.1 Annealing condition dependent structural changes

According to the results from **chapter 5.2.2**, the annealing temperatures 550℃ and 450℃ are chosen for the following experiments due to their advantage for oxygen absorption. **Figure 5.6** shows the XRD spectrum of the as-prepared powder sample R2, and the samples annealed at 550℃ and 450℃ with different annealing times. For the group at 550℃ annealed samples, only the 12h annealed LSMO powder is almost transformed to the brownmillerite but with several additional Bragg peaks. Then the sample is completely transformed after 50h. For the group of 450℃ annealed samples, the transformation speed is slower for the group of 550℃ annealed ones. However, this slower speed enables us to observe the emerging of the intermediate state. For the 450℃ 50h annealed system, the intermediate phase shows shaper Bragg peaks compared to the 30h annealed system (as shown in the orange rectangle in **Figure 5.6 (b)**). This might indicate an intermediate state with better crystallinity.

Also, after 75h annealing the brownmillerite phase can also be achieved. Combining the results from **chapter 5.2.2**, one can conclude that both too high or too low annealing temperatures decrease the oxygen getter efficiency of the aluminum. In this study, 550℃ was found to be the optimal annealing temperature.

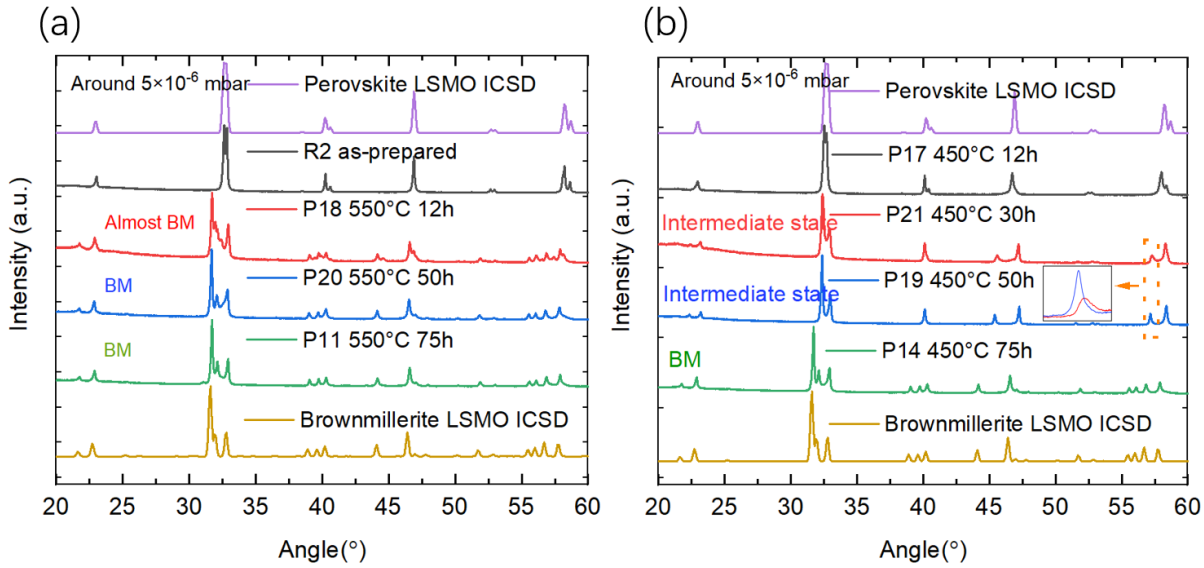

Figure 5.6 XRD spectrum of the as-prepared powder sample R2 and the annealed powder samples at different annealing temperatures and times. Panel (a) shows the XRD spectrum of the annealed samples at a fixed temperature 550℃ at various annealing times, i.e. from 12h to 75h. Panel (b) shows XRD plot of the annealed sample at a fixed temperature 450℃ at various annealing times, i.e. from 12h to 75h.

As shown in **Figure 5.7 (a)**, to verify the oxygen adsorption effect of aluminum, two samples are annealed without aluminum at 450℃ and 550℃ for 75h. Both annealed samples show an unchanged structure hereby confirming the oxygen getter effect of aluminum. When extending the vacuum pumping time to 72h, the vacuum can be further improved to reach 1.0×10^{-6} mbar (the rest in the **chapter 5.2.3** is around 5.0×10^{-6}mbar), additional two samples are annealed at this vacuum level. As in **Figure 5.7 (b)** shown, it takes only 6h for a complete PV to BM topotactic phase transition. This reveals that the vacuum condition significantly influences the transformation speed. Such short annealing time enable a planned in-situ powder neutron diffraction experiment for a real-time spin structure investigation. Moreover, the necessity of polishing the aluminum foil has been verified by sample P23.

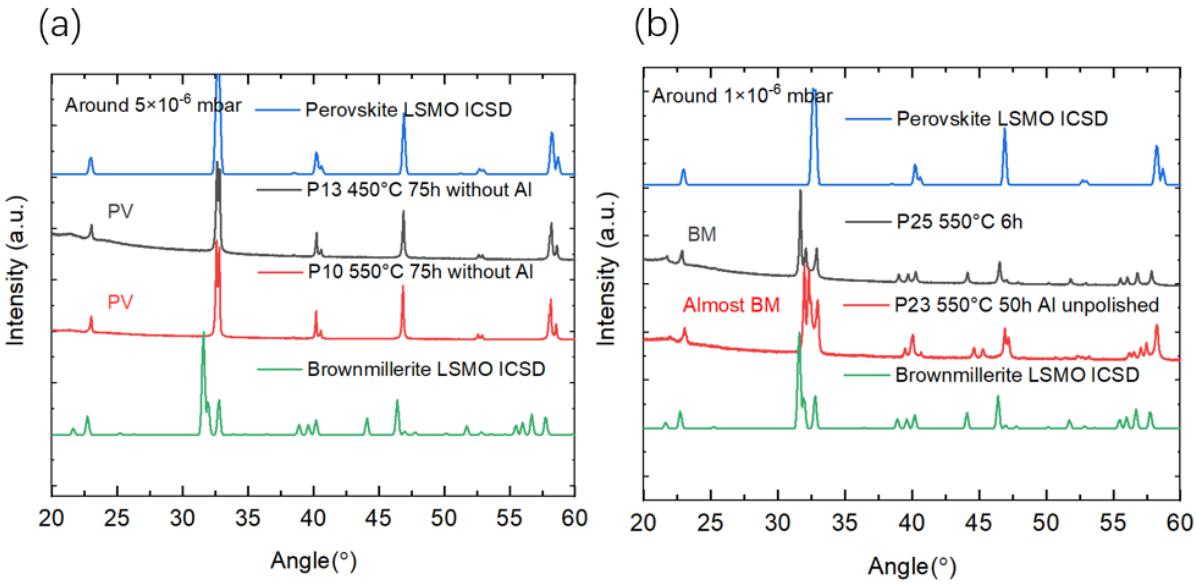

Figure 5.7 XRD spectrum of the annealed samples. (a) Annealed without aluminum. (b) Annealed in an improved vacuum.

5.2.3.2 Magnetometry measurements

Similar to the **chapter 5.2.2.2**, the field cooling curve and zero-field cooling curve are measured by SQUID magnetometry, shown in **Figure 5.8**. The ferromagnetic contribution is also calculated by normalization at 350K. From the field cooling curve, the improved intermediate state of the 450°C 50h annealed sample shows a smaller magnetization compared with the intermediate stated obtained in **chapter 5.2.2.2** (0.39% compared with 2.8%). This confirms the assumption of increased oxygen desorption and the suppressing of double exchange interactions. In addition, for the BM structure obtained from the 550°C 75h annealed sample, still a 0.14% ferromagnetic contribution is found (similar to the 0.39% of the improved intermediate state), which might originate from a core-shell structure of the powder grains with larger diameters. For the grain size of 100 nm, the transmission coefficient of $\mathrm{Cu}-\mathrm{K}_{\alpha}$ X-ray decreases to 4.2×10^{-7}. Consequently, the XRD spectrum may not show the structure inside the core. However, from the zero-field cooling curve both the improved intermediate state and the BM state show a typical anti-ferromagnetic behavior with a Néel-temperature around 55K.

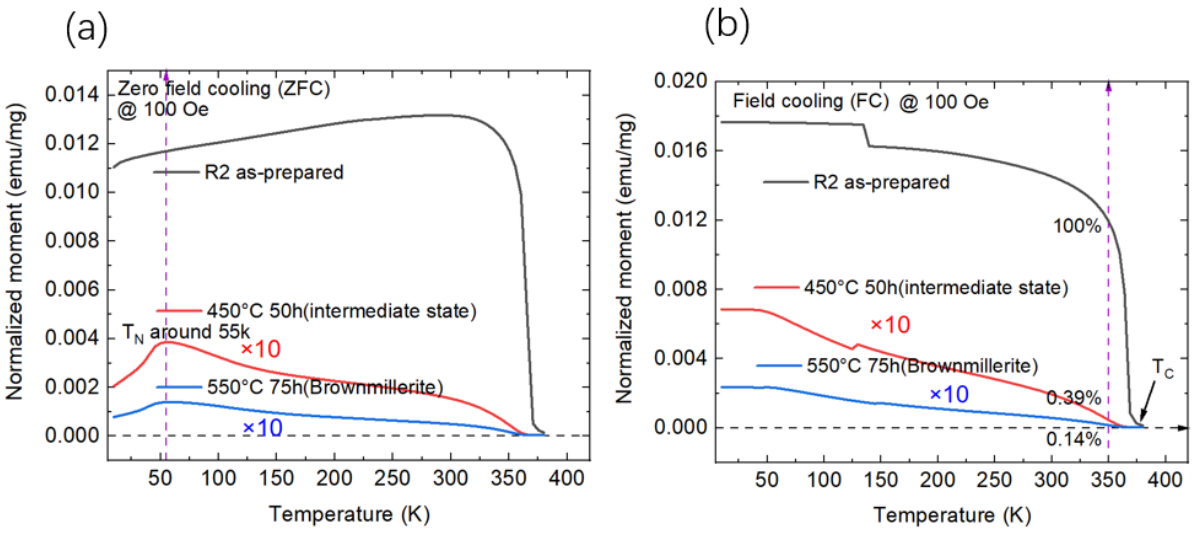

Figure 5.8 Magnetization-temperature curves of the as-prepared powder sample R2 and the annealed samples. Panel (a) shows the zero-field cooling (ZFC) curves. Panel (b) shows the field cooling (FC) curves. The amplitude of the blue and red curves is multiplied by a factor of 10 for better comparison.

5.2.3.3 Morphology (SEM) and elemental analysis (ICP-OES)

The morphology of the annealed sample (550°C 75h, brownmillerite) is characterized by scanning electron microscopy (SEM). From the overall morphology image (**Figure 5.9 (a)**), one can observe the aggregation which might due to the annealing. The grain size varies over several orders of magnitude. Moreover, from the corresponding composition contrast image (**Figure 5.9 (b)**), the material with darker contrast could be the quartz segments which has a lower electron scattering density and very likely introduced when breaking the quartz tube. The local morphology image (**Figure 5.9 (c)**) shows isolated particles, which exhibits no obvious contrast compared with the as-prepared powder sample R2 (**Figure 5.1 (f)**).

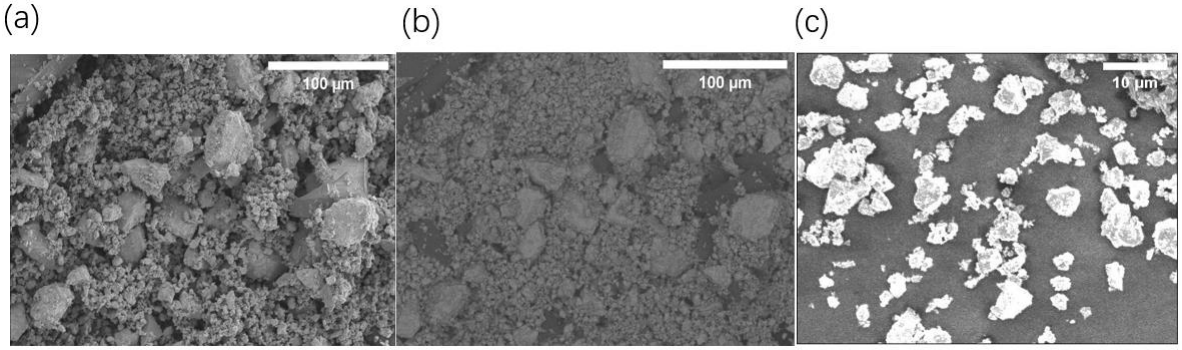

Figure 5.9 SEM images of annealed sample (550°C 75h, BM state). Panel (a), (b), and (c) show the overall morphology, overall composition contrast, and local morphology, respectively.

By inductively coupled plasma optical emission spectrometry (ICP-OES) the element content of the as-

prepared sample R2 and annealed sample is characterized. In **Table 5.1**, the La : Sr : Mn molar ratio after annealing stays almost unchanged being very close to the ratio of the sputter target (70 : 30 : 100). In addition, the background element contents (i.e., Fe and Si) stay nearly constant. However, the aluminum content significantly increases after annealing, since the annealing temperature is lower than the melting point as well as the boiling point of aluminum. This result might be explained by a contamination of the aluminum particles from the polished aluminum foil.

Table 5.1 Elemental analysis of the as-prepared sample R2 and annealed sample.

Sample ID	La [%]	Sr [%]	Mn [%]	Fe [%]	Si [%]	Al [%]	La : Sr : Mn mole ratio
R2, as-prepared	42.7 ±1.2	11.3 ±0.3	23.5 ±0.6	0.0126 ±0.0009	0.0243 ±0.0007	< 0.0006	71.87 : 30.16 : 100
P11, 550℃ 75h annealed	42.9 ±0.9	11.42 ±0.08	23.5 ±0.4	0.0116 ±0.0016	0.023 ±0.003	0.02168 ±0.00096	72.20 : 30.47 : 100

5.3 Summary

In this chapter, the aluminum-assisted vacuum annealing is performed on LSMO powder samples. By exploring the annealing temperature, time, and vacuum level, the PV to BM topotactic phase transition can be successfully triggered. Moreover, a potential intermediate state with antiferromagnetic behavior is found.

6. Summary and Outlook

This Project-thesis is the continuation of the PhD thesis of Lei Cao as well as the Master thesis of Hengbo Zhang. In the previous research, the topotactic phase transition from the as-prepared perovskite (PV) to the oxygen-deficient brownmillerite (BM) was successfully realized by vacuum annealing of LSMO thin film samples [4, 33]. Additionally, almost pure BM phases were achieved on the powder sample through aluminum-assisted vacuum annealing [33].

In this study, the thin film samples are grown by HOPSD using the same growth parameters as in Hengbo Zhang's Master study. From the XRD and XRR spectra, the as-prepared films show a thickness around 40 nm as well as a roughness of 2 to 3 nm and exhibit a good repeatability. Here first attempts of the ionic liquid gating (ILG) method on LSMO thin films are conducted. The resulting changes of topographic, structural, and magnetic properties on LSMO films are investigated. AFM studies indicate a surface decomposition after gating. XRD scans reveal an inhomogeneous lattice expansion with probably a self-passivation region. The gated films show a lower Curie temperature with a smeared-out shape in the field cooling curve and a reduced saturation magnetization accompanied by an increased coercive field. These results imply a weakened double exchange interaction due to gating. Furthermore, surprisingly, a large hydrogen content (20% to 30%) in the gated film is confirmed by NRA. One might assume that the Mn ions shift to lower oxidation states induced by the hydrogen insertion and/or oxygen vacancy formation. This also leads to a lattice expansion and the suppression of the double exchange interactions. In the next step, we plan to use a conducting substrate (Nb doped STO) to improve the film homogeneity during gating, and to directly investigate the oxygen vacancy concentration by other characterization methods (e.g. Polarized Neutron Reflectometry).

In addition, using bulk powder samples, the topotactic phase transition is investigated by adopting aluminum-assisted vacuum annealing. The samples are prepared by 30 min hand milling using an old HOPSD target, SEM images show the morphology of the as-prepared sample. The powder grain size varies over several orders of magnitude due to the inhomogeneous hand milling. By using various annealing conditions, the LSMO powder samples are successfully transformed from PV to BM at 550°C within only 6 hours. A potential intermediate state with anti-ferromagnetic behavior is found along the phase transition route. Compared with the intermediate state, the final BM phase shows a further reduced magnetization as well as anti-ferromagnetism with a Néel-temperature at around 55 K. This might be explained by the influence of oxygen vacancies onto the Mn oxidation state so that the double exchange mechanism is gradually replaced by dominating super-exchange interactions. The La : Sr : Mn stoichiometry before and after annealing is also confirmed

using ICP-OES elemental analysis. However, via a refinement of the XRD spectrum the exact identity of the intermediate phase needs to be determined. Furthermore, in the future, real-time spin-structure monitoring during an in-situ aluminum-assisted vacuum annealing by powder neutron diffraction is planned.

7. References

1. la O', G. J., et al., Catalytic Activity Enhancement for Oxygen Reduction on Epitaxial Perovskite Thin Films for Solid-Oxide Fuel Cells. Angewandte Chemie, 2010.**122**(31): p.5472-5475.

2. Petrie, J. R., et al., Enhancing Perovskite Electrocatalysis through Strain Tuning of the Oxygen Deficiency. Journal of the American Chemical Society, 2016.**138**(23): p.7252-7255.

3. Waser, R., et al., Redox-Based Resistive Switching Memories-Nanoionic Mechanisms, Prospects, and Challenges. Advanced Materials, 2009.**21**(25-26): p.2632-2663.

4. Cao, L., Controlling structural and physical properties of epitaxial transition metal oxide films through oxygen stoichiometry, PhD thesis. 2019, Forschungszentrum Jülich GmbH, RWTH Aachen.

5. Tilley, R.J.D., Perovskites: Structure-Property Relationships. 2016: John Wiley & Sons.

6. Tan, H. T., et al., 2D Transition Metal Oxides/Hydroxides for Energy-Storage Applications. ChemNanoMat, 2016.**2(**7): p.562-577.

7. Kalinin, S. V., et al., Functional Ion Defects in Transition Metal Oxides. Science, 2013.**341**(6148): p.858-859.

8. Meyer, J., et al., Transition Metal Oxides for Organic Electronics: Energetics, Device Physics and Applications. Advanced Materials, 2012.**24**(40): p.5408-5427.

9. Hemberger, J., et al., Structural, magnetic, and electrical properties of single-crystalline ($La_{1-x}Sr_xMnO_3$ $(0.4 < x < 0.85)$). Physical Review B, 2002.**66**(9): p.1-8.

10. Blundell, S., et al., Magnetism in condensed matter. 2001: Oxford University Press.

11. Moritomo, Y., et al., Antiferromagnetic metallic state in the heavily doped region of perovskite manganites. Physical Review B,1998.**58**(9): p.5544-5549.

12. Stokes, H. T., et al., Group-Theoretical Analysis of Octahedral Tilting in Perovskites. Acta Crystallographica Section B, 1998.**54**(6): p. 782-789.

13. Woodward, P. M., et al., Influence of Cation Size on the Structural Features of $Ln_{1/2}A1_{1/2}MnO_3$ Perovskites at Room Temperature. Chemistry of Materials, 1998.**10**(11): p. 3652-3665.

14. Milton, O. et al., Materials Science of Thin Films. 1992: Elsevier.

15. Reichelt, K., et al., Nucleation and growth of thin films. Vacuum, 1988. **38**(12): p. 1083-1099.

16. Venables, J.A., et al., Atomic processes in crystal growth. Surface Science, 1994. **299-300**: p. 798-817.

17. Brückel, T., et al., Neutron Scattering. 2015: Forschungszentrum Jülich GmbH.

18. Blundell, S. J., et al., Polarized neutron reflection as a probe of magnetic films and multilayers. Physical Review B, 1992.**46**(6): p.3391-3400.

19. M. I. Faley, et al., High oxygen pressure deposition and patterning methods for metal oxide heterostructures, Poster. 2012, Forschungszentrum Jülich GmbH.

20. Waschk, M., Interface phenomena in $La_{1/3}Sr_{2/3}FeO_3$ / $La_{2/3}Sr_{1/3}MnO_3$ heterostructures and a quest for p-electron magnetism, PhD Thesis. 2017, Forschungszentrum Jülich GmbH, RWTH Aachen.

21. Schmitz, M., Strain and electric field mediated manipulation of magnetism in $La_{(1-x)}Sr_xMnO_3$ / $BaTiO_3$ heterostructures, PhD Thesis. 2015, Forschungszentrum Jülich GmbH, RWTH Aachen.

22. Zakalek, P., Magnetic Interface Effects in Thin Film Heterostructures, PhD Thesis. 2015, Forschungszentrum Jülich GmbH, RWTH Aachen.

23. Voigtländer, B., et al., Scanning probe microscopy. 2015: Springer.

24. Lagar, J. H., et al., Material Contrast Identification And Compositional Contrast Mapping Using Backscattered Electron Imaging. Proceedings of the 20th IEEE International Symposium on the Physical and Failure Analysis of Integrated Circuits (IPFA), 2013: p. 464-469.

25. Lanford, W. A., et al., Analysis for hydrogen by nuclear reaction and energy recoil detection. Nuclear Inst. and Methods in Physics Research, B, 1992.**66**(1–2): p.65-82.

26. Fukutani, K. Below-surface behavior of hydrogen studied by nuclear reaction analysis. Current Opinion in Solid State and Materials Science, 2002.**6**(2): p.153-161.

27. Zhao, S., et al., Quantitative Determination on Ionic-Liquid-Gating Control of Interfacial Magnetism. Advanced Materials, 2017.**29**(17): p. 1606478.

28. Herklotz, A., et al., Reversible Control of Interfacial Magnetism through Ionic-Liquid-Assisted Polarization Switching. Nano Letters, 2017.**17**(3): p.1665-1669.

29. Ge, C., et al., Metal-Insulator Transition Induced by Oxygen Vacancies from Electrochemical Reaction in Ionic Liquid-Gated Manganite Films. Advanced Materials Interfaces, 2015.**2**(17): p.1-6.

30. Lu, N., et al., Electric-field control of tri-state phase transformation with a selective dual-ion switch. Nature, 2017.**546**(7656): p.124-128.

31. Deng, J., Large lattice mismatch effects on the epitaxial growth and magnetic properties of FePt films. Journal of Magnetism and Magnetic Materials, 2018.**446**: p. 125-134.

32. Kawasaki, M., et al., Atomic Control of the $SrTiO_3$ Crystal Surface. Science, 1994.**266**(5190): p.1540-1542.

33. Zhang, H., Influence of oxygen stoichiometry onto physical properties of $La_{0.7}Sr_{0.3}MnO_{3-\delta}$ powder and thin films, Master thesis. 2020, Forschungszentrum Jülich GmbH, RWTH Aachen.

34. Adamo, C., Enhanced electrical and magnetic properties in $La_{0.7}Sr_{0.3}MnO_3$ thin films deposited on $CaTiO_3$-buffered silicon substrates. APL Materials, 2015.**3**(6): p. 062504.

35. Kumari, S., et al., Effects of Oxygen Modification on the Structural and Magnetic Properties of Highly Epitaxial $La_{0.7}Sr_{0.3}MnO_3$ (LSMO) thin films. Scientific Reports, 2020.**10**(1): p.1-11.

36. Chen, H., et al., Thickness-driven first-order phase transitions in manganite ultrathin films. Physical Review B, 2019.**99**(21): p.1-13.

8. Acknowledgement

During the preparation of this Project-thesis, I have received a lot of invaluable helps from many people. Their comments and advices contribute to the accomplishment of the thesis.

I would like to extend my deep gratitude to the following people:

Prof. Dr. Thomas Brückel for providing me the opportunity to work at JCNS-2.

PD Dr. Oleg Petracic as my supervisor for providing me this interesting project as well as offering me numerous valuable comments and suggestions with incomparable patience throughout my Projektarbeit in the past half year.

Dr. Lei Cao for fruitful discussions, supports, and NRA measurements in HZDR.

Hengbo Zhang and **Suqin He** for various experimental training and measurements.

Dr. Ulrich Rücker and **Dr. Emmanuel Kentzinger** for their help and support in the X-ray lab of JCNS-2.

Dr. Connie Bednarski-Meinke, Yifan Xu, and **Jianwei Ye** for the help in AFM measurements.

Dr. Patrick Schöffmann and **Dr. Mai Hussein** for discussions and supports.

Dr. Felix Gunkel, and **Hong Yan** for the help of XRD measurements in PGI-7.

Dr. Shibabrata Nandi for help and support at PPMS.

Jörg Perßon and **Andreas Schwaitzer** for the assistance in powder hand milling and aluminum-assisted vacuum annealing.

Berthold Schmitz and **Frank Gossen** for technical supports on HOPSD, MPMS, and PPMS.

Finally, I would like to express my thanks to all the members at JCNS-2 for the friendly atmosphere.

Last but not least, I am very grateful to my parents for their unfailing love and support.